12-1995

Electrical Characterization of 4H-and 6H-Silicon Carbide Schottky Diodes

Jeffrey C. Wiemeri

DEPARTMENT OF THE AIR FORCE
AIR UNIVERSITY
AIR FORCE INSTITUTE OF TECHNOLOGY

19970606 103

Wright-Patterson Air Force Base, Ohio

DTIC QUALITY INSPECTED 1

AFIT/GAP/ENP/95D-16

ELECTRICAL CHARACTERIZATION OF
4H- AND 6H-SILICON CARBIDE
SCHOTTKY DIODES

THESIS

Jeffrey C. Wiemeri, 2nd Lieutenant, USAF

AFIT/GAP/ENP/95D

The views expressed in this thesis are those of the author and do not reflect the official policy or position of the Department of Defense or the U.S. Government

AFIT/GAP/ENP/95D-16

ELECTRICAL CHARACTERIZATION OF 4H- AND 6H-SILICON CARBIDE
SCHOTTKY DIODES

THESIS

Presented to the Faculty of the Graduate School of Engineering

of the Air Force Institute of Technology

Air University

in Partial Fulfilment of the

Requirements for the Degree of

Master of Science in Engineering Physics

Jeffrey C. Wiemeri, B.S.
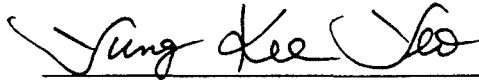
2nd Lieutenant, USAF

December 1995

ELECTRICAL CHARACTERIZATION OF 4H- AND 6H-

SILICON CARBIDE SCHOTTKY DIODES

Jeffrey C. Wiemeri, B.S.
2nd Lieutenant, USAF

Approved:

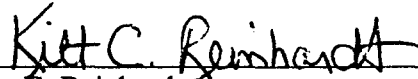_Yung Kee Yeo_   30 Nov. '95

Yung Kee Yeo
Chairman, Advisory Committee

Robert L. Hengehold   30 Nov '95

Robert L. Hengehold
Member, Advisory Committee

Kitt C. Reinhardt   1 Dec '95

Kitt C. Reinhardt
Member, Advisory Committee

Acknowledgments

I would like to express my deepest thanks to a team of people who have made this thesis project a success. First, I would like to thank Dr. Yung Kee Yeo and Dr. Robert Hengehold for their quality teaching and guidance that inspired me to study solid state physics. I would next like to thank Dr. Kitt Reinhardt who sponsored my thesis and who lent invaluable time and information, let alone use of his facilities for experimentation. Appreciation goes to all the committee members for their views of the thesis from conception to completion. Their corrections, critiques, and input were crucial in obtaining a high quality work that reflects well on the whole thesis team. Thanks also goes to Mr. Jim Scofield, who did the DLTS tests for me and who figured out the Richardson's constant problem, Lt. Mike Dunn, who aided me greatly by acquainting me with the equipment I would be using, and Mr. Chris Tunstall, who helped me keep the equipment running. Finally, I would like to thank my newlywed wife, Kiley Elizabeth, for her unwavering love and support.

<div align="right">Jeffrey C. Wiemeri</div>

Table of Contents

List of Tables

List of Figures

Abstract

The electrical properties of silicon carbide (SiC) make it an excellent candidate for use in high temperature/high power devices due to its wide bandgap, high breakdown field, high electron mobility, etc. In this work two Schottky diodes of platinum (Pt) on n-type carbon faced 4H-SiC and three Schottky diodes of nickel (Ni) on n-type silicon faced 6H-SiC were electrically characterized. The diodes exhibited good performance up to 698 K for both the forward and reverse (up to -100V) bias voltages. The barrier heights measured by I-V-T tests were found to be 0.32 and 0.61 eV for the Pt/4H-SiC samples, but 1.08, 1.10, and 1.13 eV for the Ni/6H-SiC samples. Current voltage dependencies of thermionic and field emission were compared to theory and the diode current characteristics were found to have large tunneling and series resistance components. The series resistance for the Pt/4H-SiC and Ni/6H-SiC samples were determined to be about 70 Ω and 60 Ω, respectively. The ideality factors were found to decrease with temperature as predicted by theory, and ranged from n=3.2-1.6 and n=2.2-1.0 for the Pt/4H-SiC and Ni/6H-SiC samples, respectively. This determined that the Pt/4H-SiC diodes had a larger tunneling component. The Richardson's constant-active area products were found to be much smaller than theoretically calculated, indicating that the effective active areas much smaller than the contact and/or large quantum mechanical tunneling and reflection components are present. Capacitance tests revealed carrier concentrations of approximately 5×10^{16} cm^{-3} in the Pt/4H-SiC samples and 3×10^{17} cm^{-3} in the Ni/6H-SiC samples. The barrier heights determined from capacitance measurements were found to be

1.5-2 eV and 4-9 eV for the Pt/4H-SiC and Ni/6H-SiC samples, respectively. Differences between current and capacitance results are attributed to the reverse bias band bending, defects on the contact surface, and the high carrier concentration of the Ni/6H-SiC samples. Activation energy analysis found traps at about 50, 150, and 450 meV in the 4H-SiC samples and about 300 and 400 meV in the 6H-SiC samples. The 50 meV level is attributed to the nitrogen donor in the h-site of the 4H-SiC lattice. Breakdown voltages obtained at room temperature were ~140V and ~500V for the 4H- and 6H-SiC samples, respectively. Application of Fluorinert on the Ni/6H-SiC samples was found to increase the breakdown voltage to ~800V. It is concluded that silicon faced, lower doped, edge-insulated contacts will give better results in future SiC Schottky diode studies.

1. Motivation

1.1 Silicon Carbide for High Temperature/High Power Devices

Silicon carbide (SiC) is a wide bandgap semiconductor that is currently of high interest to the U.S. Air Force, the Department of Defense, and to electronic device manufacturers in general. The reason for this interest is that the physical and electrical properties of SiC make it an excellent candidate for use in electronic devices operating in conditions too extreme for current silicon (Si) based technology. Such conditions include high temperature, high frequency, high voltage, and high radiation environments. These environments are typical of those encountered on aircraft and space vehicles.

In an aircraft, aero-heating of aircraft surfaces can cause temperatures to reach as high as 250 °C, while engine areas can reach as high as 350 °C, or even higher. With present Si devices, the method of dealing with these adverse environments is to either place the electronics far from the source and remotely monitor the systems, which decreases the signal to noise ratio, or to include large environmental control units (ECU's) that actively cool the electronics. Active cooling relies on the hydraulics of an aircraft. As military systems continue to develop, the projected thermal loads on the electronics will increase, thus necessitating larger hydraulic systems. Support for the hydraulics in an aircraft constitutes a major portion of the maintenance work and equipment necessary for aircraft operation, and as larger hydraulic systems are required, the costs become enormous (1).

Presently, the Air Force is pursuing the More Electric Aircraft (MEA) initiative. With this initiative, electronics will be used in power management and distribution, actuator motor control, on-site smart sensors, and data bus electronics, replacing current hydraulic operations. These devices will need to be able to operate in the harsh environments mentioned above, without the aid of the ECU's. Thus the devices will need to be able to operate at high temperature and power (1). Such devices would be of use in spacecraft and weapons systems as well because weight dedicated to cooling systems could be eliminated. Thus, much sought after redundancy in spacecraft could be employed where it currently is not feasible, and weapons can carry larger payloads and improved guidance systems.

While Si is MILSPEC design limited to 125 °C, using silicon-on-insulator technology, devices have been created to operate up to 250-300 °C. However, this is short of the MEA requirements where devices will need to run reliably at temperatures as high as 400 °C (1). Thus new semiconductor devices need to be made that can operate under these conditions. These devices will be made of wide bandgap semiconducting materials, so that higher temperatures can be reached before the doped material becomes intrinsic (where the electrons being excited from the valence band to the conduction band exceeds greatly the number of electrons donated from the impurities) (2:4).

While a wide bandgap is necessary for all materials considered, important properties that distinguish materials for use are Hall and drift mobilities, electron saturation drift velocities, carrier lifetimes, and dielectric constants. Processing properties, such as the availability of a substrate, ability to form stable contact metallizations, purity of

growth samples, and the ability to dope the materials are also major considerations when choosing a material (2:9).

Silicon carbide is unique in that it has multiple crystal configurations called polytypes. Due to the different crystal structure, the polytypes differ in electronic properties. The most common and applicable polytypes of silicon carbide are 3C-, 6H- and 4H-SiC. Table I lists some properties of the current candidates for high temperature electronics as compared to Si. A large advantage of silicon carbide over the other materials is its ability to form silicon oxides. This makes it compatible with current silicon technology. Also, due to the progress of substrate and epitaxial growth in the past five years, the 4H- and 6H- polytypes of silicon carbide have become the front runners for use in high power, high temperature, and high frequency electronic devices.

1.2 Importance of Schottky Diodes

A Schottky diode is a type of metal-semiconductor (MS) device. MS devices are based upon the contact of a metal to a semiconductor. If the MS contact demonstrates rectifying characteristics, it is called a Schottky contact, however if it shows linear nonrectifying characteristics, it is an ohmic contact. The defining property of a Schottky contact is the barrier height (ϕ_B) formed when the metal is brought into contact with the semiconductor. In ideal Schottky contacts, the barrier height depends on the work functions of the metal and semiconductor used. However, if a large density of surface states is present on the semiconductor surface, the barrier height depends on the properties of the semiconductor surface, and is independent of the type of metal used.

3

Ohmic contacts are used to connect semiconductor materials with the circuitry of a system (5:8-16).

Table I. Summary of electrical properties of various wide bandgap semiconductors (3;4:37-38).

Property	Silicon	GaAs	GaN	3C-SiC	4H-SiC	6H-SiC
Bandgap	1.1	1.4	3.39	2.2	3.2	3.0
Physical Stability	Good	Fair	Good	Excellent	Excellent	Excellent
Electron Mobility RT, cm^2/Vs	1400	8500	900	1000	720	600
Hole Mobility RT, cm^2/Vs	600	400	150?	60	60	60
Breakdown Voltage E_b, 10^6 V/cm	0.3	0.4	5?	4	4	4
Thermal Conductivity c_T, W/cm	1.5	0.5	1.3	2.6	5	5
Dielectric Constant ε_0	11.8	12.8	9	9.7	9.7	9.7

The most important devices using Schottky contacts include metal semiconductor field-effect transistors (MESFETS), solar cells, and diodes. A Schottky diode is the simplest of these devices consisting of the metal contacted to an n- or p-type semiconductor. Schottky diodes are used as saturation-prevention clamps for high-speed bipolar integrated circuits, discrete high frequency diodes for signal detection and

4

amplification circuits in microwave communication systems, and as diagnostic tools to study the doping profiles, deep level defects, energy-density of states relationships of the semiconductor material, and the characteristics of the Schottky contact itself. Schottky diodes are also used, to a lesser extent, as load resistor substitutes, diode couplers, level shifters, gates for microwave transistors, and as optical or nuclear detectors (5:3-4). Unlike pn diodes in which the minority carrier current is the dominant mechanism, Schottky diodes utilize high speed majority carrier conduction. This, coupled with the lower turn on voltages of Schottky diodes, allows for higher switching speeds and lower power losses than in a pn diode (6:2).

Due to the need for well-behaved metal-semiconductor contacts in device fabrication, it is of primary importance that the MS contact properties of a material be completely understood. Fabrication and study of Schottky diodes made from a material under consideration for device application will greatly add to the understanding needed in forming successful devices. Current-voltage, capacitance voltage, deep level transient spectroscopy, and breakdown voltage tests are some of the common methods used to characterize the properties of Schottky diodes.

1.3 Silicon Carbide Schottky Diodes

Schottky diodes made with silicon carbide have been researched since the 1960's. However, there has been a renewed interest in the study of silicon carbide MS contacts due to the promising aspects of silicon carbide's use in high temperature and high power devices. It has been found that many metals form Schottky contacts with silicon carbide.

5

Both annealed and unannealed contacts have been studied, and barrier height values were obtained. Table II lists the metals, annealing temperature, and barrier heights of recently studied 4H- and 6H-SiC Schottky contacts.

Prototype silicon carbide devices utilizing Schottky contacts have been made, but degradation of the metal contacts limits the lifetime of the devices to only a few hours when the devices are operated at temperatures near 600 °C in atmospheric environments (7). The degradation mechanism is thought to be caused by oxidation, as shown by tests that extend device lifetimes to 55 hours at 600 °C under vacuum (7). Also, at high temperatures, metal-contact interdiffusion and electromigration, along with oxidation, can occur. Thus metal-semiconductor and metal-metal reactions play a large role in determining the ability of Schottky contacts to withstand the harsh environments that will be encountered by high temperature/high power devices.

A great amount of research has been done in looking at the metal contact degradation mechanisms in silicon and III-V devices. However, there has been comparatively little research done with silicon carbide. This is especially true with high temperature degradation studies. To date the details of Schottky contact formation are not yet fully understood (7).

Besides low contact degradation, a large barrier height is desired in the formation of stable high temperature Schottky contacts. It has been found that the metal and polytype of silicon carbide used, and whether or not the contact was annealed plays a large part in determing ϕ_B (7).

Table II. Schottky Contacts to n-type 4H- and 6H-SiC (7).

Contact Metallization	SiC Type	Annealing Temp.	SBH (eV)	Year Published	Ref.
Ni	6H, C-face	as-deposited	2.2	1992	9
"	6H,Si-face	"	1.5	"	9
Au	6H	"	2	"	10
Ti	6H, Si-face	"	0.88	"	11
"	6H, Si-face	700 °C-1 hr.	1.04	"	11
Pd	6H, C-face	as-deposited	1.6	"	12
"	6H,Si-face	"	1.11	"	"
Au	6H,C-face	"	1.14	"	"
"	6H,Si-face	"	1.4	"	"
Ag	6H,C-face	"	1.1	"	"
"	6H,Si-face	"	0.92	"	"
Mn	6H,Si-face	"	0.81	"	"
Al	6H,C-face	"	0.84	"	"
"	6H,Si-face	"	0.3	"	"
Mg	6H.C-face	"	0.33	"	"
"	6H,Si-face	"	0.3	"	"
Pt	6H	"	rectifying	"	13
Ti	6H,C-face	"	1.0	1993	14
"	6H,C-face	400 °C	0.98	"	"
"	6H,Si-face	as-deposited	0.73	"	"
"	6H,Si-face	400 °C	0.97	"	"
Ni	6H,C-face	as-deposited	1.59	"	"
"	6H,C-face	400 °C	1.66	"	"
"	6H,Si-face	as-deposited	1.24	"	"
"	"	400 °C	1.25	"	"
"	"	600 °C	1.39	"	"
Al	6H,C-face	as-deposited	0.84	"	"
"	"	600 °C	1.66	"	"
"	6H,Si-face	as-deposited	0.3	"	"
"	"	600 °C	1.12	"	"
Ti	"	as-deposited	0.85	"	8
Pt	"	"	1.02	1993	"
Au	4H,Si-face	"	1.73	1995	15
Ni	"	"	1.60	1995	"
Ti	"	"	1.10	"	"
"	4H	"	0.99	"	16

This indicates that MS contacts made with silicon carbide do not posses many surface states and that the formation of carbides and silicides under annealing affects the barrier height. On the other hand, some studies have shown that barrier heights are unaffected by the metal used, which would indicate the presence of surface states (8). Therefore, the method of preparation as well as the materials used are both key factors in determining the behavior of silicon carbide Schottky diodes.

1.4 Purpose of Research

Before SiC Schottky contact devices can be made to withstand the necessary environments, more research into the degradation mechanisms and the properties of the Schottky contacts needs to be done. In aid to this endeavor, the purpose of this research was to characterize Schottky diodes made with platinum deposited on 4H-SiC and nickel deposited on 6H-SiC. The Pt/4H-SiC Schottky diodes were obtained from an outside contractor and the Ni/6H-SiC Schottky diodes were made by the University of Cincinnati. Current-voltage-temperature (I-V-T), capacitance-voltage-temperature (C-V-T), capacitance-frequency-temperature (C-f-T), deep level transient spectroscopy (DLTS), and breakdown voltage tests were performed. Schottky barrier heights, doping profiles, trap activation energies, current mechanisms, and breakdown voltages were determined.

1.5 Organization of Thesis

This thesis is organized as follows. Chapter one is dedicated to giving a brief synopsis of the reasons the research in SiC Schottky diodes is being conducted, what has

been learned and what still needs to be done. Chapters two and three are dedicated to giving background and theory behind silicon carbide and Schottky diodes respectively. Chapter four describes the theory, the procedures and the equipment used to test the diodes. Chapter five gives the results of the experiments and an analysis of these results. Chapter six finishes the thesis by providing conclusions made from the analysis and recommendations for future studies.

2. Background on Silicon Carbide

2.1 Crystal and Band Structure of Silicon Carbide

Silicon carbide was one of the first semiconductors discovered and is the most known member of a group of close-packed materials that exhibit a one-dimensional polymorphism called polytypism. The polytypes of SiC are differentiated by the stacking sequence of the tetrahedrally bonded Si-C bilayers. The nearest neighbors are the same for all the polytypes, such that individual bond lengths and local atomic environments are nearly identical, however differences arise when the second and third nearest neighbor atoms are considered. These differences lead to different stacking periodicity which determines the overall symmetry of the crystal. A nearly infinite number of possible polytypes exist, so a shorthand has been developed to catalogue the structures.

Each bilayer of SiC, while maintaining the tetrahedral bonds, can be situated in one of three possible positions with respect to the lattice, denoted as A, B, or C. The three polytypes of SiC being considered for device applications are the 3C-, 4H-, and 6H-SiC. The H or C term refers to the hexagonal or cubic symmetry of the crystal, respectively. The 3, 4, and 6 refer to the bilayer periodicity (3). Within the sublattices of the multilayer polytypes there are crystollographically non-equivalent atoms. These are denoted by an "h" or a "k". Atoms of h-type are in an hexagonal environment, while those of k-type are in a cubic environment. Numerical subscripts are used to differentiate atoms of the same type, but in different crystalline positions (4). Figure 1 and Table III show the crystal structure and stacking sequences of the 4H- and 6H-SiC polytypes.

10

Table III. Stacking sequences of common SiC polytypes (4:33).

Polytype	ABC Notation	# Inequivalent sites	# Cubic Sites	# Hexagonal Sites
3C(zincblende)	ABC	1	1	0
4H	ABAC	2	1	1
6H	ABCACB	3	2	1

3C-SiC is the only cubic SiC, and it has a zincblende structure. It is often called b-SiC. All other polytypes are denoted as a-SiC. The unit cell dimensions of the polytypes are a = b = 3.078 Angstroms, c = n x 2.518 angstroms. Where n is the bilayer periodicity number (2:11). 6H-SiC, with stacking sequence ABCACB, is the most commonly occurring polytype of silicon carbide. It has a larger bandgap, reported as 2.86-3.0 eV at 300 K (18;3) than that of 3C-SiC (zincblende), 2.2eV. However, its electron mobility is not as high (3). 4H-SiC, with a stacking sequence of ABAC, has the widest bandgap of the three, 3.2 eV (19:49), and an electron mobility close to that of 3C-SiC. 4H-SiC holds the most promise for device applications, but it is behind 6H-SiC in development.

As mentioned earlier, a large band gap is desired in materials considered for high temperature, high power applications. The reason for this is that when operating at higher temperatures, the reverse leakage currents, I_{rev}, of pn diodes cause a degradation in MOS device (i.e. MOSFETs) threshold voltage and noise-margin results. Also, the substrate, I_{sub}, and gate leakage currents of horizontal devices (i.e. JFETs, MESFETs) cause a degradation in transconductance and frequency response when operating at high temperature. The gate leakage currents are due to the degradation of Schottky contacts

as stated before. However, the I_{rev} and I_{sub} currents originate from a thermally generated intrinsic carrier concentration, n_i, which is exponentially dependent upon temperature and the energy band-gap of the semiconductor material (1), as shown by:

$$n_i = \sqrt{N_c N_v}\, e^{\frac{-E_g}{2kT}}, \tag{2.1}$$

where N_C is the density of states of the conduction band and N_V is the density of states of the valence band, k is Boltzman's constant, E_g is the energy bandgap, and T is the absolute temperature. N_C and N_V are given by:

$$N_c \equiv 2(\frac{2\pi m_{d,e} kT}{h^2})^{3/2} M_c, \tag{2.2}$$

and $\quad N_v \equiv 2(\frac{2\pi m_{d,h} kT}{h^2})^{3/2}, \tag{2.3}$

where $m_{d,e}$ and $m_{d,h}$ are the density of state effective masses for electrons and holes, respectively. The I_{rev} and I_{sub} currents go approximately as (1):

$$\begin{aligned} I_{rev} &\propto n_i \\ I_{sub} &\propto (n_i + N) \end{aligned} \tag{2.4}$$

where N is the doping density.

The energy band structures of 4H and 6H silicon carbide are quite complex compared to the structure of silicon and other common semiconductors due to the number of atoms in the unit cells. None the less, the band structure has been calculated by Junginger and van Haeringen (20) and by V.I Gavrilenko et al. (21). Junginger and van Haeringen used the empirical pseudopotential method, while V.I Gavrilenko et al.

calculated the band structure by the first-principles self-consistent linear muffin-tin orbital (LMTO ASA) method. Their results are shown in Figure 2. It is standard to expect that there are six equivalent conduction band minima in 4H- and 6H-SiC that contribute to electron transport (22). This minimum occurs on the ΓM line and the bandgap for both 4H and 6H SiC is indirect.

Theoretically the effective mass of the carriers of a semiconductor is determined from the energy band structure in momentum space. The effective mass is tensorial, and in a given direction in momentum (k) space is given by:

$$\frac{1}{m_{i,j}^*} \equiv \frac{1}{\hbar^2} \frac{\partial^2 E(k)}{\partial k_i \partial k_j} \qquad (2.5)$$

Experimentally the effective masses, $(m_\perp, m_\parallel)$, for the 4H- and 6H-SiC electrons are $(0.176m_0, 0.224m_o)$ and $(0.24m_o, 0.34m_o)$, respectively (22). The perpendicular and parallel effective masses refer to the values calculated transverse to the symmetry axis and along the symmetry axis, respectively. The density of states effective mass,

$$m_{d,e}^* = (m_\perp^* \, m_\parallel^*)^{1/3}, \qquad (2.6)$$

in the conduction band is thus $0.19m_0$ for 4H-SiC and $0.27m_0$ for 6H-SiC. It is considered to be independent of temperature (23).

When impurities are substituted into the inequivalent lattice sites of a respective polytype, different electronic properties are seen. The most abundant impurity, introduced in the growth process, is nitrogen.

When nitrogen replaces atoms at lattice sites, three different ionization energies are observed in 6H-SiC and two in 4H-SiC. This is due to the one hexagonal (h) site and two cubic (k_1, k_2) sites in 6H-SiC, and the one hexagonal and one cubic (h,k) sites in 4H-SiC. The ionization energies for the nitrogen donors for h- and k-sites in 4H-SiC are 51.8 and 91.4 meV, respectively. For 6H-SiC, the ionization energies for the h-, k_1-, and k_2-sites are 81,137.6 and 142.4 meV, respectively (22).

2.2 Epitaxial and Bulk Growth of Silicon Carbide

At present the most common method for growing silicon carbide substrate material is through a modified version of a sublimation process introduced by Lely in 1955 (24). In Lely's process, crystal growth occurred in cylindrical graphite crucibles. The growth zone of the crystals consisted of an apertured thin-walled graphite cylinder. The starting material was powdered SiC synthesized from pure Si and C. The crucible was heated, and crystals were grown in an inert gas (usually argon) atmosphere at approximately 2500 °C. The nucleation of crystals took place in the growth zone, mainly in the holes of the graphite tube (4:51).

In the modified Lely sublimation process, SiC is transported in the vapor phase to a SiC seed crystal held at a lower temperature (25). In this method, nucleation occurs at the seed crystal attached to either the top or bottom of a cylindrical growth cavity (see figure 3). Similar to the Lely process, SiC sublimes from a polycrystalline source to produce Si, Si_2C, and SiC_2. These diffuse through a porous graphite retainer and along carefully programmed thermal and pressure gradients.

16
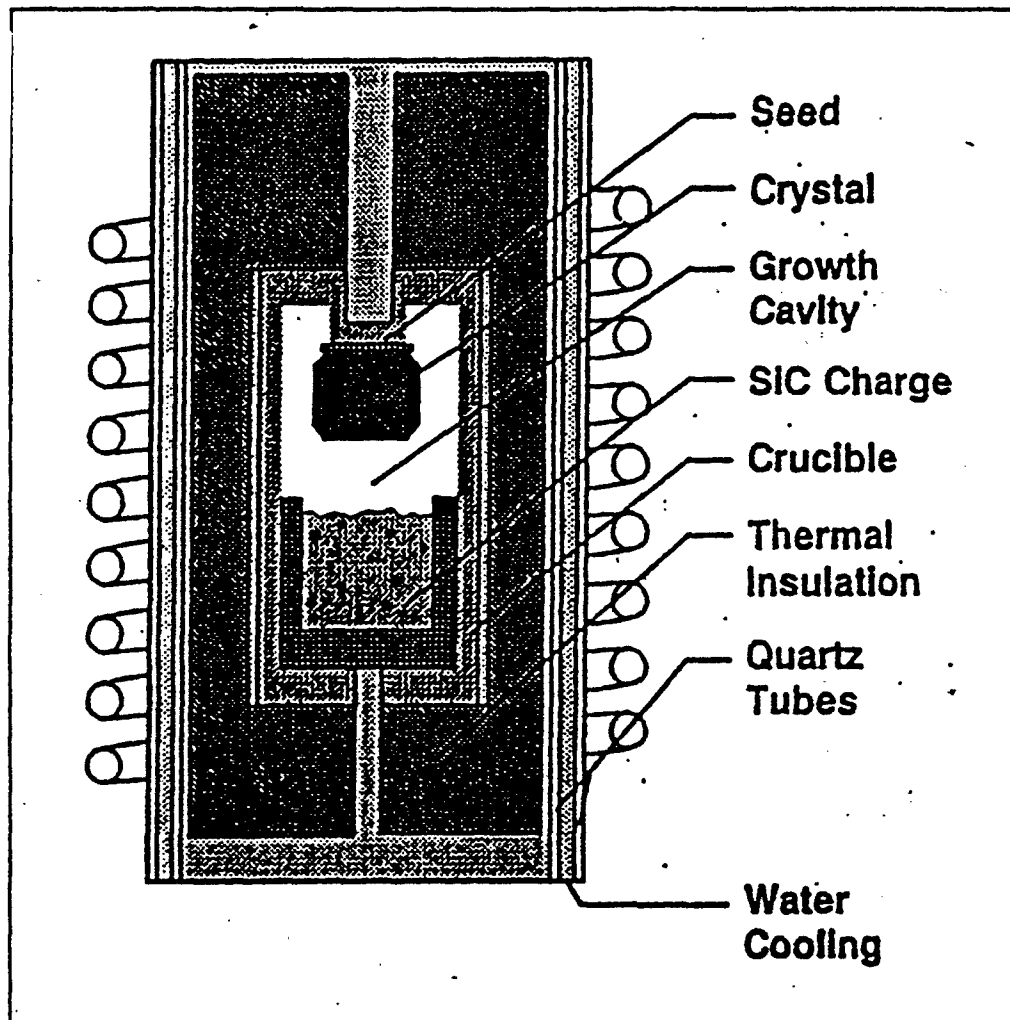
Figure 3. Typical SiC sublimation growth apparatus (26:8)

The main gaseous species, silicon, reacts with the graphite walls of the cylinder forming additional Si_2C and SiC_2. Thus, the silicon acts as a carbon transporting agent, playing an active role in the formation of the species impinging on the growing crystal. This process, like the original, is done in an argon atmosphere. A seed crystal temperature of about 1800 °C and a source temperature of around 2000 °C are typical (3). For accelerated growth rates, seed crystal temperatures of 2200 °C and source temperatures of 2300 °C under a pressure of 5 torr has been done (27), and other temperature combinations in the 2000 °C area are not uncommon. Wafers are then cut from the resulting boule. Cree Research Inc. and the North Carolina State University developed this technique with Navy funding during the 1980's. In 1989, the first one-inch diameter 6H-SiC wafers became available (1). 2" wafers are now commercially available in both 6H and 4H polytypes, and 3" wafers are expected by 1997 (28). This ability to grow high quality, single polytype substrates of both 4H- and 6H-SiC is the main reason that SiC leads other wide bandgap materials in device technology.

Impurity levels in the SiC crystals depend upon the impurity content of the source material and the seed crystal, the quality of graphite parts, and the purity of the argon atmosphere. Due to the high temperatures involved, almost all metals (Al, Ti, V, Cr, Ni, Fe, etc.) act as contaminants due to their high vapor pressures in the growth chamber (29:7-9). Due to the inability to get 100% pure argon and the impossibility of pulling a complete vacuum, nitrogen retains a presence in the growth chamber as well. Intentional doping is achieved by adding aluminum or boron to the source mixture to obtain p-type material, and introducing a partial pressure of high purity nitrogen to obtain n-type

18

material. In the case of nitrogen, the donor concentration increases with the partial pressure, (P_{N2}), as (4:51):

$$N_D = 6.5 \times 10^{18} \sqrt{P_{N_2}}.$$
(2.7)

The size of the SiC crystals is limited by the ability to cut large diameters of very hard material, and the appearance of tiny hexagonal voids that extend the length of the boule. These "tubes" in the material are known as micropipes, and they are observed to nucleate at the seed crystal. Two possible formation mechanisms for micropipes have been put forth (30). The first suggests that micropipes are open core super screw dislocations that propagate along the C-axis from the seed crystal during growth. The second theory is that contaminant particles, such as carbon inclusions or silicon droplets on the growth face (28), introduced in the growth process cause the formation of micropipes. The diameter of a micropipe varies depending on the formation mechanism, but usually is 0.5 to 10 μm. Cree Research Inc. has limited the density of micropipes to under 100 cm^{-2} (28). However, the densities of micropipes must be further reduced. Micropipes have been established as a defect limiting the areas of high-voltage devices to under a few mm^2. At present levels, micropipes will limit the performance of large size silicon carbide power devices to under that of existing silicon devices.

The controlled growth of high-quality epilayers is a key issue in the quest for SiC devices. Early epitaxial growth of SiC was done by liquid phase epitaxy (LPE) or by sublimation. Presently, chemical vapor deposition (CVD) has replaced both LPE and sublimation as the epitaxial growth method (3). In CVD, gaseous chemicals are introduced into the growth chamber where they react to give off SiC that crystallizes with

the substrate SiC crystal. Polytype matching is achieved by polishing the substrate wafer at a 3-4° angle off the (0001) basal plane (31). This polishing forces the epilayer growth to take place at the abundance of growth surface steps. Thus, the polytype of the substrate is mirrored in the epilayer.

Dopants can be added similarly by the introduction of various chemical elements and compounds that react to give off the desired dopants that then are crystallized within the substrate. Low pressure CVD has been done, when using large Si substrates, but atmospheric pressure CVD provides adequate uniformity when using the small SiC substrates. This in-situ doping is primarily achieved through the introduction of gaseous nitrogen or aluminum (31).

3. Background and Theory of Schottky Diodes

3.1 Historical Overview of the Schottky Diode

In 1874, rectification in metal-semiconductor diodes was first observed by Braun (32). The devices he used consisted of a metal point contacted to lead sulfide and iron sulfide semiconductors. Development of these first devices led to the MS point contacts being used as radio detectors. From 1905 until 1925, the "point contact crystal rectifier" was the main type of radio detector in the market. Their use was supplanted by vacuum tube technology, and the rectifiers were limited to u.h.f. detection in the lab.

With the onset of the second world war and the development of microwave radar, the point contact diode once again gained importance. It served as a frequency converter and low level microwave detector, offering lower noise operation and better detection of low level microwave square-pulses than the vacuum tube. Development of MS point contact rectifiers during the war helped lead to the invention of the transistor.

During the 1950's, the MS point contact diode once again took a back seat, as pn diodes were being developed. The use of the MS contact was limited to operation as an ohmic contact to carry current into the pn diodes. The pn diodes gave better performance and were more understood than their metal-semiconductor counterparts. However, in the 1960's, with the invention and development of the planar process, MS diodes were researched heavily and new uses found. With the ability to form a plane versus point contact of metal to the semiconductor, the interfaces became more predictable, and their use expanded dramatically. As mentioned earlier, the uses of planar MS, or Schottky,

diodes include operation as clamping diodes to enhance switching speed of bipolar integrated circuits, operation as microwave diodes, or as gates of microwave transistors.

During the 1970's with the boom in the computer and electronics industry, the demand for higher frequency and faster switching components led to further development of Schottky diodes. Due to such development, the Schottky diode currently enjoys many uses as mentioned in the first chapter.

3.2 Schottky Barrier Formation and Energy Band Structure

The ideal Schottky barrier depends only on the work functions of the materials used. The work function (in volts) of the metal, ϕ_M (in volts), and the semiconductor, ϕ_S, is the energy required to remove an electron from the respective Fermi levels to vacuum. As shown in Figure 4, the electron affinity, X_S, and the energy difference, V_n, between the conduction band and the Fermi level of the semiconductor relate to the work function as:

$$\phi_S = X_S + V_N.$$

(3.1)

The value V_N is determined by:

$$V_N = \frac{kT}{q}\ln(\frac{N_C}{n_e}),$$

(3.2)

where n_e is the density of electrons in the conduction band. In this ideal case, the contact will demonstrate rectifying behavior when the semiconductor work function is less than the metal work function, $\phi_S < \phi_M$. If $\phi_M < \phi_S$, then the contact will be ohmic and will demonstrate linear current-voltage characteristics (5:11-14). Rectifying MS contacts, are discussed in this section.
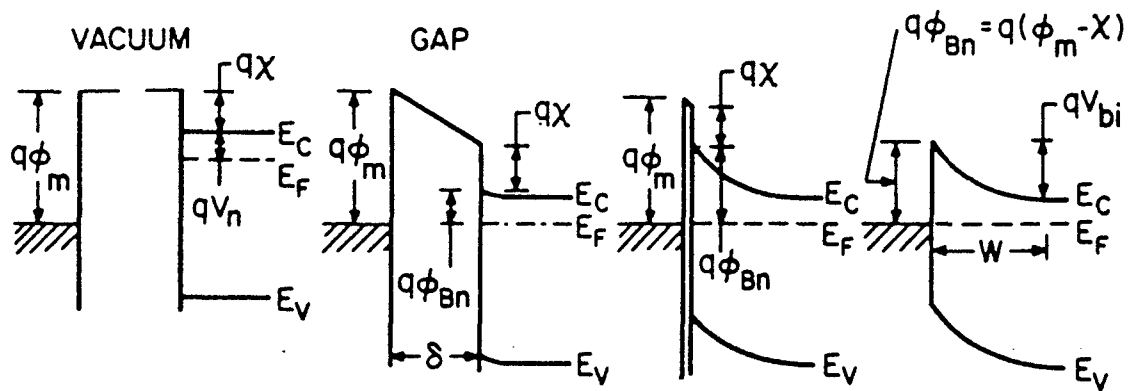
Figure 4. Energy band formation of a metal-semiconductor contact (33:247).

At a large distance, flat energy bands are observed (5:11) (see Figure 4). This implies that the semiconductor terminates at the surface without distorting the energy levels, thus leaving no surface states. When a metal is brought in contact with an n-type semiconductor, the contact potential (the difference between the Fermi levels) will cause the electrons to flow from the semiconductor to the metal. Thermal equilibrium is achieved when the Fermi levels match. This transfer of electrons builds up negative charge in the metal and an equal and opposite charge from positive donor ions forms at the semiconductor surface. The resulting dipole field opposes further transfer of electrons, and a barrier is established as shown in Figure 4. The barrier height, ϕ_B, is

defined as the energy difference between the Fermi level in the metal and the bottom of the conduction band at the semiconductor-metal interface. The limiting value for the barrier height in an n-type semiconductor is thus (in electron volts):

$$q\phi_{Bn} = q(\phi_M - X_S).$$
(3.3)

For p-type material, the equation is slightly different since the Fermi level rises as electrons flow from the metal into the semiconductor,

$$q\phi_{Bp} = E_g - q(\phi_M - X_S).$$
(3.4)

The above ideal case is often referred to as the Schottky limit. However, semiconductors often posses many surface states. Surface states are electronic states at the surface capable of trapping carriers, and can be donor or acceptor-like. In equilibrium, electrons occupy the surface states of the semiconductor up to a level ϕ_0.

Between most metal-semiconductor contacts, a thin, natural, insulating oxide layer exists. As the metal is brought into contact with the semiconductor, the contact potential will cause the surface states to form a counter potential within the oxide layer. This will reduce the size of the barrier formed. If there are enough surface states to accommodate the potential difference, then the Fermi levels at the surface will become "pinned" at ϕ_0. The barrier equation (in eV) becomes:

$$q\phi_B = E_g - q\phi_0.$$
(3.5)

Thus, the barrier height is independent of the work function of the metal, and becomes solely a function of the semiconductor's bandgap and surface. This limit is referred to as the Bardeen limit.

An effect of electrons approaching the metal from the semiconductor is that image charges are formed in the metal. These charges form a potential that in essence lowers the barrier height (33:250). The Schottky effect is the image-force-induced lowering of the barrier. If an external electric field is applied in conjunction with this lowering force, the total potential energy as a function of distance, x , is (in eV):

$$PE(x) = \frac{q^2}{16\pi\varepsilon_s x} + qE_M x .$$

(3.6)

In this equation, ε_s is a proper permittivity term, and E_M is the maximum electric field at the interface. The Schottky barrier lowering, $\Delta\phi$, and the location of the lowering, x_M, occur at d[PE(x)]/dx=0. Figure 5 illustrates the Schottky barrier lowering in the energy band diagram.
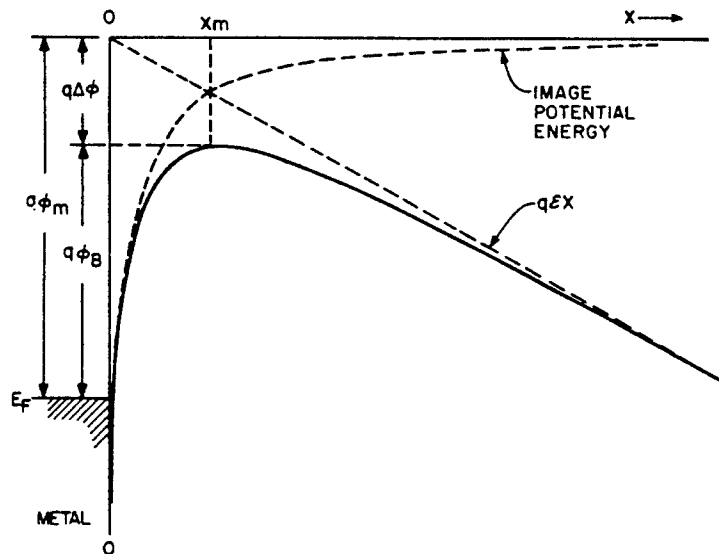
Figure 5. Energy band diagram of Schottky barrier lowering. The metal workfunction is $q\phi_m$ (33:250).

25

The resultant Schottky barrier lowering is

$$\Delta\phi = \sqrt{\frac{qE_M}{4\pi\varepsilon_s}} .$$ (3.7).

The permittivity term will be different than the static permittivity if the electron transit time from the MS interface to the barrier maximum, x_M, is less than the dielectric relaxation time. The semiconductor will not have enough time to become polarized and a smaller permittivity will result.

Often semiconductors do not meet either the Schottky or the Bardeen limit. In this general case, the barrier height is given by (33:273):

$$\phi_B' = a(\phi_M - X_S) + (1-a)(\frac{E_g}{q} - \phi_0) - \Delta\phi \equiv a\phi_M + b,$$ (3.8)

where a and b are constants to be determined experimentally. The density of surface states, D_S, is given by:

$$D_S = \frac{(1-a)\varepsilon_i}{a\delta q^2},$$ (3.9)

where ε_i is the interfacial layer permittivity, and δ is the thickness of the interfacial layer. By plotting the barrier heights of rectifying MS contacts with a certain semiconductor versus the work functions of different metals used, the constants a and b can be determined by a linear fit. The two limiting cases are:

1. $a \to 1$, then $D_S \to 0$. This means there are no surface states and equation (3.8) reduces to:

$$q\phi_B' = q(\phi_M - X_S) - q\Delta\phi \qquad (3.10)$$

This is of course the Schottky limit.

2. $a \to 0$, $D_S \to \infty$. This means there are a relatively infinite number of surface states, and equation (3.8) reduces to:

$$q\phi_B' = (E_g - q\phi_0) - q\Delta\phi. \qquad (3.11)$$

The barrier height is independent of metal used because of Fermi level pinning, and this indicates the Bardeen limit.

Figure 6 shows the plots of the barrier height versus work function for various unannealed Schottky contacts of 4H-SiC and 6H-SiC using the data in Table II and the experimentally determined workfunctions (34). The least square straight fit line to the data yields a= 0.57, b= -1.34 and a= 1.12, b= -4.63, for 4H- and 6H-SiC, respectively, where a and b are the line parameters from equation (3.8). Assuming the interfacial layer's thickness is of atomic dimensions (5 angstroms) and the permittivity is about the same as for free space ($\varepsilon_i \cong \varepsilon_0 = 8.8542 \times 10^{-12}$ Fm^{-1}), equation (3.9) gives $D_s = 8.3 \times 10^{12}$ states/cm^2/eV for 4H-SiC. The density of surface states is about one-fifth of that of Si or GaAs Schottky contacts. This indicates that 4H-SiC follows the Schottky limit more closely than these materials, therefore controlling Schottky barrier heights would be easier. The "a" value obtained for 6H-SiC indicates a very strong dependence on the workfunction of the metal.
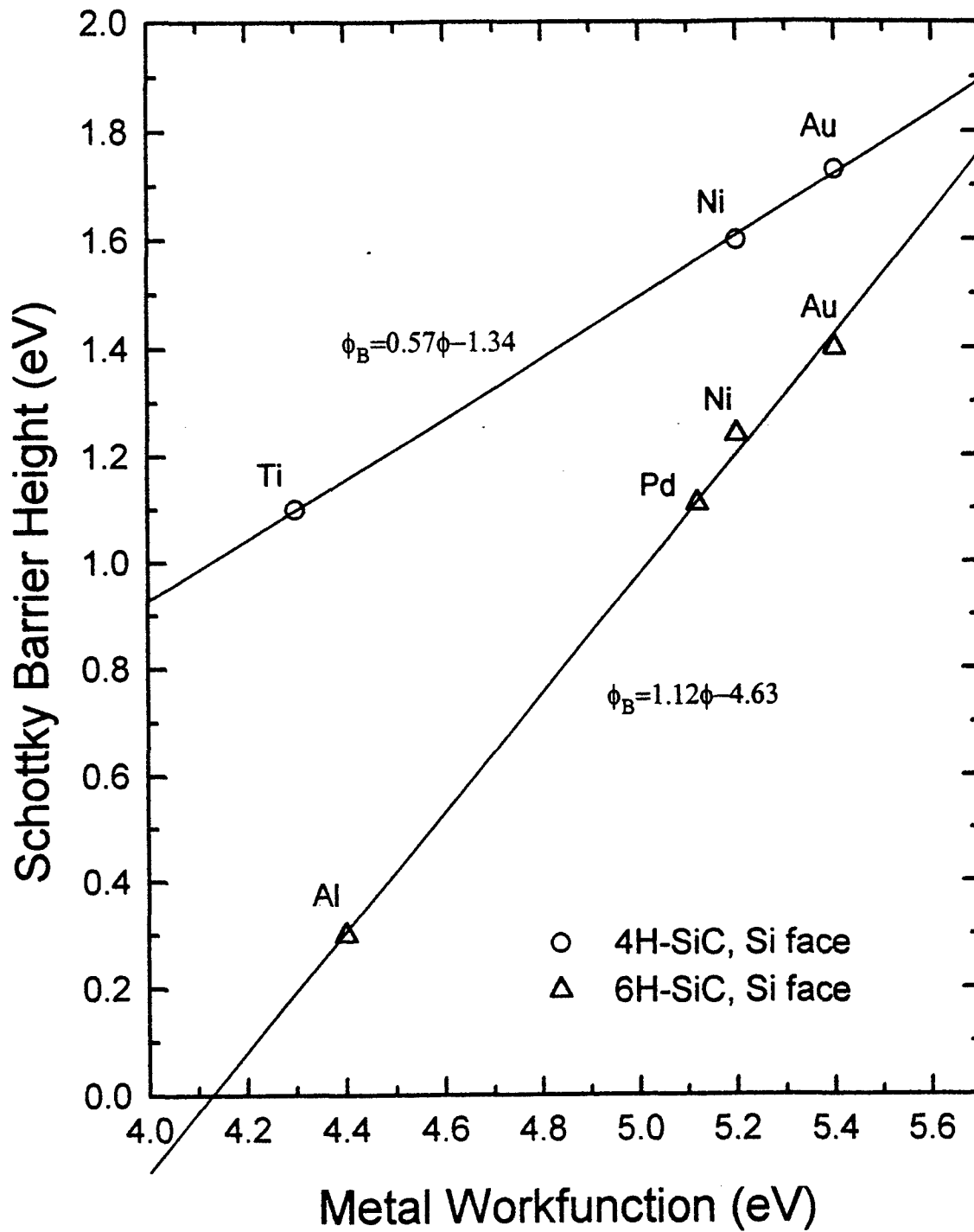
Figure 6. Plot of barrier height versus workfunction for unannealed contacts to 4H-SiC and 6H-SiC.

6H-SiC, therefore, follows Schottky theory even more. However, different fabrication and annealing techniques can cause the barrier height dependence on the workfunction for both of these materials to breakdown.

The band bending that occurs in a MS contact creates a built-in potential that the electrons in the semiconductor must overcome in order to enter the metal by thermionic emission or diffusion. This built-in potential, qV_{bi} (eV), is the difference between the unlowered barrier height and the energy difference between the conduction band and the Fermi level in the semiconductor, that is:

$$V_{bi} = \phi_B - V_n \qquad (3.12)$$

This potential is often called the contact potential, and is similar to the contact potential between the p- and n-type materials in a pn junction.

The relationship between the conduction and valence bands in the semiconductor and the Fermi level in the metal act as boundary conditions that allow one to solve Poisson's equation (33:248). This allows the determination of the width, W, of the depletion region and the capacitance that is set up at the interface. The depletion layer is similar to an abrupt (p^+-n) junction. Therefore, solving the equations:

$$\nabla \cdot D = \rho(x), \qquad (3.13)$$

$$-\frac{\partial^2 V}{\partial x^2} \equiv \frac{\partial E}{\partial x} = \frac{\rho(x)}{\varepsilon_S}, \qquad (3.14)$$

$$-\frac{\partial V^2}{\partial x^2} = \frac{qn_e}{\varepsilon_S} \quad \text{for } 0<x<W, \qquad (3.15)$$

$$-\frac{\partial V^2}{\partial x^2} = 0 \quad \text{, and} \quad \frac{\partial V}{\partial x} = 0 \text{ for x>W,} \tag{3.16}$$

and by integrating (3.15) and (3.16), one obtains an electric field, E, as:

$$|E(x)| = \frac{qn_e}{\varepsilon_S}(W - x) \tag{3.17}$$

with a maximum electric field, E_M, occurring at x=0. Integrating (3.17) gives a potential :

$$V(x) = \frac{qn}{\varepsilon_S}(Wx - \frac{1}{2}x^2) - \phi_B. \tag{3.18}$$

The built in potential and the bias voltage, V, relate to E_M as:

$$V_{bi} - V - \frac{kT}{q} = \frac{1}{2}E_M W. \tag{3.19}$$

The kT/q term is a correction factor that comes from the dipole moment of the majority-carrier distribution tail of the electrons in the n-type material. Solving equations (3.17) and (3.19) for W, one obtains:

$$W = \sqrt{\frac{2\varepsilon_S}{qn_e}(V_{bi} - V - \frac{kT}{q})} = \sqrt{\frac{2\varepsilon_S}{qn_e}(\phi_B - V_n - V - \frac{kT}{q})}. \tag{3.20}$$

The maximum electric field at the MS interface is thus given by:

$$E_M = \sqrt{\frac{2qn_e}{\varepsilon_S}(V_{bi} - V - \frac{kT}{q})}. \tag{3.21}$$

The space charge, Q_{SC}, per unit area that forms in the depletion layer is written as:

$$Q_{SC} = \sqrt{2q\varepsilon_S n_e(\phi_B - V_n - V - \frac{kT}{q})} = qnW \tag{3.22}$$

30

The capacitance per unit area, C is given by:

$$C \equiv \frac{|\partial Q_{SC}|}{\partial V} = \sqrt{\frac{q \varepsilon_S n_e}{2(\phi_B - V_n - V - \frac{kT}{q})}} = \frac{\varepsilon_S}{W}. \quad (3.23)$$

3.3 Current Transport Processes

Assuming operation under the Schottky limit, there are four main current transport mechanisms (33:254). The most dominant mechanism for rectifying contacts is the flow of electrons over the built-in potential barrier into the metal, which includes thermionic emission and diffusion indicated by 1 in Figure 7. The most significant current source for ohmic contacts and for heavily doped material is from quantum-mechanical tunneling of electrons through the potential barrier indicated by 2 in Figure 7. The third source is from recombination in the space-charge region as in a p-n junction indicated by 3 in Figure 7. The fourth source is from minority-carrier injection from the metal into the semiconductor, which is equivalent to recombination in the depletion region, indicated by 4 in Figure 7. Other sources include edge leakage currents and interfacial currents from traps at the MS contact.

Bethe developed the thermionic emission theory which bases current flow solely upon the height of the barrier (35). In his theory, he assumes that the potential barrier height is much larger than kT, that thermal equilibrium is established at the plane that
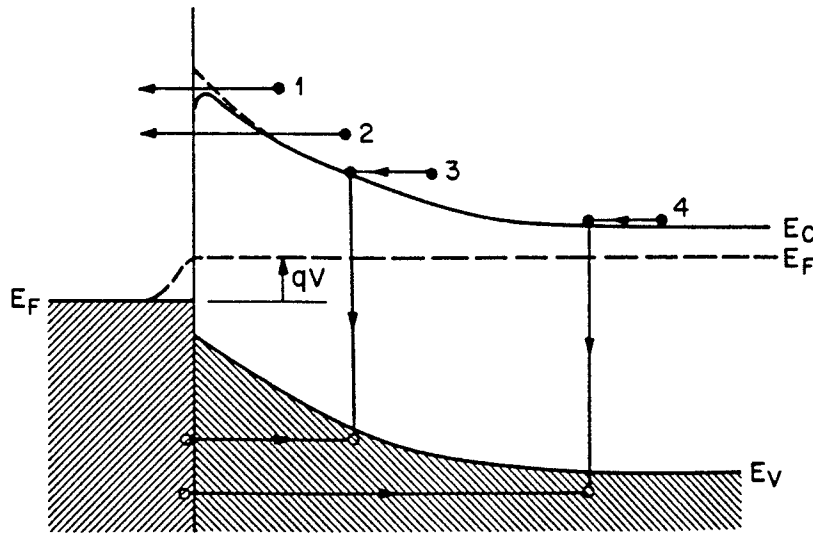
Figure 7. The four basic current transport processes in a Schottky contact (33:254). 1) Themioinc emission, 2) Tunneling, 3) Recombination in the space-charge region, 4) Minority-carrier injection.

determines emission, and that a net current flow does not affect the equilibrium, so that

opposing current fluxes may be superimposed. These assumptions make the shape of the

barrier immaterial, and current flow is regulated by the barrier height. The current that

results is from the transport of electrons over the barrier. This model neglects the drift

and diffusion of carriers caused by collisions within the space-charge region. The current-

voltage relationship for thermionic emission is given by:

$$I = [AA * T^2 \exp(-\frac{q\phi_B'}{kT})][\exp(\frac{qV}{kT}) - 1] \qquad (3.24)$$

$$= I_S[\exp(\frac{qV}{kT}) - 1], \qquad (3.25)$$

where

$$I_S = AA^* T^2 \exp(-\frac{q\phi_B{}'}{kT}).$$
(3.26).

Here A is the active area of the contact, T is the temperature, k is Boltzman's constant, I is the current, I_S is the saturation current, ϕ_B' is the Schottky barrier height, V is the applied voltage, and A* is the Richardson's constant. The Richardson's constant associated with a single energy minimum is given by (36):

$$A_1^* = 4\pi \frac{qk^2}{h^3}(l^2 m_y^* m_z^* + m^2 m_z^* m_x^* + n^2 m_x^* m_y^*)^{1/2},$$
(3.27)

where l, m, and n are the direction cosines of the normal to the emitting plane relative to the principal axes of the ellipsoid, and the m* values are the components of the electron effective mass tensor. For a free electron, A*=120A/cm²/K². For actual semiconductors, including 4H-SiC and 6H-SiC, the Richardson's constant is different.

Since both the 6H-SiC and 4H-SiC are hexagonal, and the metal is contacted on the (0001) and (000-1) face, respectively, the emitting plane is the A face of the Brillouin zone as shown in Figure 8.

Usually, for both the 4H- and the 6H-SiC, the conduction band minima occur at the M faces of the hexagon. Thus, there are six equivalent conduction band minima. (4H-SiC is sometimes noted as having 12 conduction band minima when two ellipsoids occur symmetrically on the M-L line. (2x6=12), but 6 conduction minima will be assumed here.)
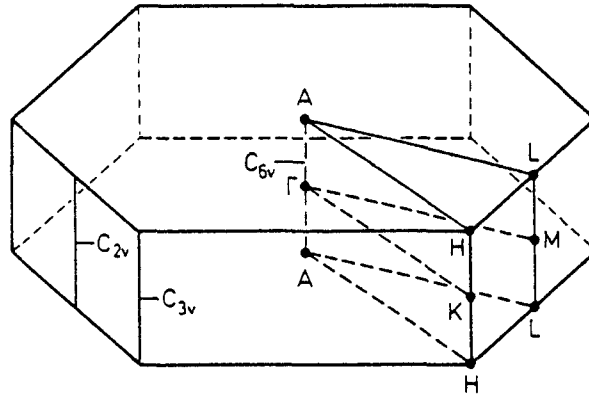
Figure 8. Brillouin zone diagram for hexagonal SiC (4:36).

Since these faces are oriented 90° to the emitting plane, the direction cosine is one for the principal, longitudinal axis of the ellipsoid that is directed towards the center of the hexagon, and one for one of the transverse axes. The direction cosine for the other transverse axis is zero. Therefore two terms in equation (3.27) drop. Since the band minima are equivalent, the Richardson's constant for each minimum is the same. Thus the complete Richardson's constant is:

$$A^* = 120 \text{x} \frac{\left(m_\parallel m_\perp\right)^{1/2}}{m_0} \text{x} 6 = 720 \text{x} (0.176 \text{x} 0.224)^{1/2} = 143 \frac{A}{cm^2 K^2},$$

where m_0 is the electron rest mass, $m_\parallel$ is the longitudinal effective mass, and $m_\perp$ is the transverse effective mass. Similarly, the Richardson's constant calculated for 6H-SiC is 206 A/cm^2/K^2

The diffusion theory by Schottky (37) is based on the assumptions that the barrier height is much larger than kT, the effects of electron collisions within the depletion region are included, the carrier concentrations at the boundary of the depletion region are unaffected by current flow, and that the impurity concentration within the semiconductor is nondegenerate. The current-voltage relationship of this theory is:

$$I \cong A[qN_C \mu E \exp(-\frac{q\phi_B}{kT})][\exp(\frac{qV}{kT}) - 1], \qquad (3.28)$$

where E is the electric field at the interface and μ is the carrier mobility.

A theory that combined thermionic emission and diffusion current processes was proposed by Crowell and Sze (38). Their theory is derived from the boundary condition of a thermionic recombination velocity, v_R, near the metal-semiconductor interface. Because diffusion is dependent upon the shape of the potential in the region diffusion occurs, they consider the shape of the electron potential energy, $q\psi(x)$ (in eV) versus distance from the interface, incorporating the Schottky lowering effect as shown in Figure 9. A charge density within the depletion region equivalent to that of the ionized donors is also assumed. An applied voltage, V, between the metal and the semiconductor bulk gives rise to a flow of electrons from the metal into the semiconductor. The current density between x_M and W is given by:

$$J = -q\mu n \frac{d\phi_n}{dx}, \qquad (3.29)$$

where μ is the mobility, and ϕ_n is the quasi-fermi level. They assume that the portion of the barrier between x_M and the interface, as shown in Figure 9, acts as a sink for

electrons. The current flow can then be expressed in terms of an effective recombination velocity, v_R, at the potential energy maximum as:

$$J = q(n_M - n_0)v_R,$$
(3.30)

where n_M is the electron density at x_M for when current is flowing, and n_0 is a quasi-equilibrium electron density which occurs if it were possible to reach equilibrium without altering the position of the potential energy maximum. The electron densities are given by:

$$n_0 = N_C e^{-q\phi_{Bn}/kT},$$
(3.31a)

$$\text{and} \quad n_m = N_C e^{[(-q\phi(x_M) - q\phi_{Bn})/kT]},$$
(3.31b)

where ϕ_{Bn} is the Schottky barrier height, and $\phi(x_M)$ is the quasi-Fermi level at the potential energy maximum.

Given $\phi(W) = -V$, combining equations (3.29), (3.30), and (3.31), and integrating $\phi(x)$ between x_M and W, one obtains:

$$I = A\frac{qN_C v_R}{1 + v_R/v_D}\exp(-\frac{q\phi_{Bn}}{kT})[\exp(-\frac{qV}{kT}) - 1],$$
(3.32)

where v_D is an effective diffusion velocity associated with the transport of electrons from the edge of the depletion layer at W to the potential maximum at x_M, and is defined as

$$v_D \equiv [\int_{x_M}^{W} \frac{q}{\mu kT}\exp[-\frac{q}{kT}(\phi_{Bn} + \psi(x))]dx]^{-1}.$$
(3.33)

Figure 9. Energy band diagram of Schottky contact incorporating Schottky barrier lowering. The electron potential energy is $q\psi(x)$, and the quasi-Fermi level is $q\phi(x)$ (33:260).

Assuming a Maxwellian distribution of the electron density for $x \geq x_M$ and that no electrons return from the metal except those associated with qn_0v_R, the semiconductor acts as a thermionic emitter. Thus, v_R, the thermal recombination velocity is given by

$$v_R = \frac{\int_0^\infty v_x \exp\left(-m^*v_x^2/2kT\right)dv_x}{\int_{-\infty}^\infty \exp\left(-m^*v_x^2/2kT\right)dv_x} = \left(kT/2m^*\pi\right)^{1/2} = \frac{A^*T^2}{qN_C}, \quad (3.34)$$

where A* is the effective Richardson's constant. From equation (3.32), it is seen that if v_D >> v_R, then the first term is dominated by v_R, and thermionic emission theory most applies, but if v_R >> v_R, then the diffusion process is dominant. If image-force lowering were neglected, and if the mobility were independent of the electric field, E, then v_D would simply be equal to μE. In this case, if the diffusion process were dominant, then the current density would be equivalent to the current density from diffusion theory, as shown in Equation (3.28). If image-force lowering was included, however, then the potential, $\psi(x)$, would be:

$$\psi(x) = \phi_B' + \Delta\phi - Ex - \frac{q}{16\pi\varepsilon_S x}, \qquad (3.35)$$

where ϕ_B' is the lowered barrier height, and $\Delta\phi$ is the barrier lowering. Using Equation (3.35) instead for v_D still yields a value of $v_D \cong \mu E$ for $\Delta\phi < kT/q$. However, v_D reduces to 0.3 μE when $\Delta\phi$ is increased to 20kT/q.

The Richardson's constant discussed earlier does not account for backscattering of electrons from optical-phonon reactions, for quantum-mechanical reflection from the barrier, or for tunneling through the barrier by electrons. These effects distort the assumed Maxwellian distribution for calculation of v_R. To include these effects, an adjusted Richardson's constant is given by (38):

$$A** = \frac{f_p f_Q A*}{1 + f_p f_Q \dfrac{v_R}{v_D}}, \qquad (3.36)$$

where f_p is the probability of electron emission over the potential maximum averaged over a Maxwellian distribution. The f_p is given by:

$$f_p = \int_0^\infty f_p(E,T)\exp(-E/_{kT})dE\,/\,kT, \qquad (3.37)$$

where E in this case is the energy of the electron. A first approximation of f_p is:

$$f_p = \exp(-x_m/_\lambda), \qquad (3.38)$$

where λ is the mean free path of the electron. f_Q is the ratio of current flow including tunneling and reflection effects to current flow neglecting these effects, and is given by:

$$f_Q = \int_{-\infty}^\infty \tau \exp(-E\,/\,kT)dE\,/\,kT, \qquad (3.39)$$

where E is the energy of the electron, and τ is the transmission coefficient. The transmission coefficient of carriers incident on Schottky barriers is discussed by Crowell and Sze (39). The transmission coefficient can be determined as:

$$\tau = \left|\frac{E}{A}\right|^2 \frac{m_1}{m_2}, \qquad (3.40)$$

where E/A equals the ratio of the transmitted Wentzl, Kramers and Brillouin (WKB) wave to the incident WKB wave and m_1 and m_2 are the effective masses of the carrier in the first material and the second material where the carrier was transmitted into, respectively. Thus, under thermionic theory, a complete current-voltage relationship is given by:

$$I = I_S(e^{qV/kT} - 1), \qquad (3.41a)$$

and
$$I_S = AA^{**}T^2 \exp(-\frac{q\phi_{Bn}}{kT}). \qquad (3.41b)$$

39

Tunneling, also known as field emission, is an important current transport process and can significantly alter the current-voltage characteristics. It most often occurs for high dopings and low temperatures. Under thermionic emission theory, additional tunneling effects can be incorporated by changing the current equation to:

$$I = I_S(e^{qV/nkT} - 1),$$ (3.42)

where n is the ideality factor which equals one if no tunneling effects are present. If the applied voltage $V \gg kT/q$, then the exponential term dominates and (3.42) can be rewritten as:

$$I = I_S e^{qV/nkT},$$ (3.43)

where n and I_S can be determined experimentally by plotting the natural log of I versus V. I_S is found by extrapolating the linear region to V=0, and n is found from the slope of the linear region and is defined as:

$$n \equiv \frac{q}{kT} \frac{\partial V}{\partial(\ln I)}.$$ (3.44)

If the ideality factor is much greater than one then tunneling effects are dominant. Internal physical effects can also cause n to deviate from unity. For instance, the image-force lowering, $\Delta\phi$, affects n as shown by (40):

$$n = \frac{1}{1 - \Delta\phi/4E},$$ (3.45)

where E is the electric field at the interface.

The tunneling component of current goes as (33:265):

40

$$I_t \sim e^{-q\phi_{Bn}/E_{00}}, \qquad (3.46)$$

where E_{00} is a characteristic energy defined as:

$$E_{00} \equiv \frac{q\hbar}{2}\sqrt{\frac{N_D}{\varepsilon_S m^*}}. \qquad (3.47)$$

Here $\hbar$ is Planck's constant divided by 2π, and N_D is the doping density. With increasing doping density, the depletion width, W, decreases, thus field emission increases. Lower temperatures also result in higher tunneling probabilities. A useful ratio is the thermal energy, kT, to the characteristic energy, E_{00} (7). When $kT/E_{00} \gg 1$, thermionic emission currents dominate the current flow, for $kT/E_{00} \approx 1$, both thermionic emission and field emission are dominant, for $kT/E_{00} \ll 1$, tunneling processes dominate, as shown in Figure 10.
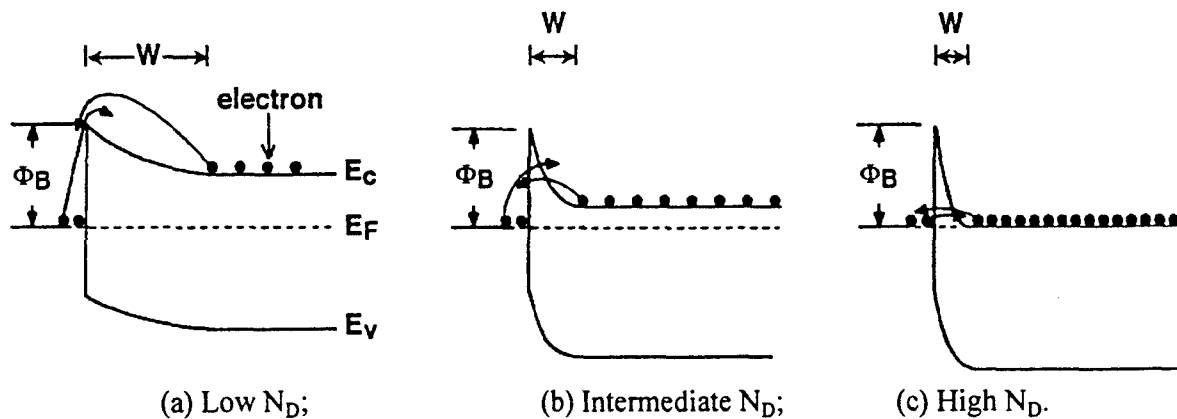

Figure 10. Illustration of current flow mechanisms. a) Thermionic emission. b) Thermionic-field emission. c) Field emission (7).

The third significant current transport process is from recombination in the space-charge region. This is identical to the recombination currents in a pn junction. Under forward bias the recombination current goes as:

$$I_{rec} \sim \exp[\frac{qV}{2kT}] \ . \tag{3.48}$$

The fourth current process is minority carrier (hole) injection from the metal into the semiconductor. This is equivalent to recombination in the neutral region. The injection ratio, γ, is the ratio of minority-carrier current to total current,

$$\gamma \equiv \frac{J_p}{J_p + J_n} \ . \tag{3.49}$$

Here J_p and J_n are the current densities from hole and electron currents, respectively. The current density equation for the minority (hole) carriers is:

$$J_p = q\mu_p p_n E - qD_p \frac{\partial p_n}{\partial x} \ . \tag{3.50}$$

The first term is the drift component, and the second term is the diffusion component. D_p is the minority carrier diffusion constant, p_n is the hole density in the semiconductor, E is the electric field at the interface, and μ_p is the hole mobility.

Under low injection conditions (low forward bias) the minority carrier diffusion term dominates. Assuming this and that the diffusion length of the holes is larger than the depletion region, the hole current density can be written as:

$$J_p = \frac{qD_p}{W} p_n[\exp(\frac{qV}{kT}) - 1] = \frac{qD_p}{W}\frac{n_i^2}{n_e}[\exp(\frac{qV}{kT}) - 1], \tag{3.51}$$

42

where n_i is the intrinsic carrier concentration, and p_n is given by:

$$p_n = \frac{n_i^2}{n_e}.$$

(3.52)

Equation (3.49) can then be written as:

$$\gamma \cong \frac{J_p}{J_n} = \frac{q n_i^2 D_p}{n_e L_p A^{**} T^2 \exp(^{-q\phi_{Bn}}/_{kT})}$$

(3.53).

With larger forward bias γ increases due to the enhancement of the drift-field component of the current compared to the diffusion current. If the continuity and transport equations are solved, the injection ratio is found to be a constant, γ_0, up to a critical current density, J_0, and from there it increases linearly with the current. γ_0 and J_0 are given by (41),

$$\gamma_0 \equiv \frac{q D_p n_i^2}{n_e W J_s},$$

and

$$J_0 \equiv \frac{q D_n n_e}{W},$$

(3.54)

where D_p and D_n are the diffusion coefficients for electrons and holes, respectively, and J_S is the saturation current density.

The other major current-voltage characteristic comes from the resistance of the contact. A Schottky diode will have two characteristic resistances. One is the specific contact resistance, and the other is the series resistance of the contact. The specific contact resistance, R_C, is the characterizing parameter for ohmic contacts. It is defined as

the reciprocal of the derivative of current density with respect to voltage evaluated at zero bias (42), as shown by:

$$R_C = \left(\frac{\partial J}{\partial V}\right)^{-1}_{V=0}. \qquad (3.55)$$

For ohmic contacts a small specific contact resistance is desired so that the linear current-voltage characteristics are due to the series resistance of the MS contact. In a Schottky diode, a large specific contact resistance is desired in comparison to the series resistance. The series resistance is the resistance from the small interfacial oxide layer at the contact and the resistance from the bulk semiconductor material. If this layer becomes too large, series resistance will begin to dominate, and the contact will develop ohmic behavior. For a Schottky contact with a large series resistance, the series (forward) resistance has a linear relation with the current, and at large forward voltages, this resistance will dominate and give a linear current voltage relationship.

The other current transport processes of edge leakage currents and interface currents due to traps at the interface can often be removed by proper manufacturing to give a good contact of semiconductor to metal, and by use of high resistive material to remove edge current paths.

3.4 Present Development of Silicon Carbide Schottky Diodes

The recent interest in SiC Schottky diodes has led to research into various metals and processing techniques. As mentioned in the first chapter, many metals readily form Schottky contacts with SiC, and the processing techniques are very important in

44

establishing good contacts that have few interfacial defects. This section will discuss some of the current processing techniques, and some of the results obtained from the samples made by these processes.

The first step in making a good Schottky contact is in proper preparation of the wafer surface prior to deposition (7). Contaminants on the surface can reduce adhesion of metals to SiC and increase contact resistance. These contaminants and any native oxide layer must be removed before metal deposition can occur. Common solvents such as trichloroethylene (TCE), trichloroethane (TCA), acetone, methanol, and propanol are used to degrease the SiC wafer. To obtain an oxide free surface, A. Evwaraye et al. (43) and M.I. Chaudhry et al. (44) suggested growing a thermal oxide layer, and then removing it by acid etching just before metal deposition. This procedure was also successful in removing surface defects caused by mechanical polishing. Acids used for etching include HF, H_2SO_4, HCl, $NH_4OH:H_2O_2:H_2O$, $HCl:H_2O_2:H_2O$, $H_2SO_4:H_2O_2$, $HNO_3:H_2SO_4:H_2O$, K_2CO_3, and KOH melt. In-situ surface cleaning is also done by sputter etching or irradiation by a high-energy laser prior to metal deposition.

Some of the most common techniques used for metal deposition include sputtering, evaporation, chemical vapor deposition (CVD), and molecular-beam epitaxy (MBE). Sputtering is a well established technique based on the bombardment of a target with energetic ions. The target's surface atoms are released, and land on the wafers to become part of the film coating. With the evaporation technique, the deposition material is vaporized from its liquid phase, and the vapor is transported and deposited on the wafer. This technique is done in a strong vacuum, so that the vapor is able to avoid collisions

45

with residual gas, thus enabling the vapor direct travel to the wafer. A nucleation and growth process condenses the vapor onto the wafer.

Chemical vapor deposition (CVD), as described earlier, uses volatile compounds containing the deposition species as transport agents. The agents are reacted on the surface of the wafer creating the desired deposit. Excellent step coverage and selectivity are two reasons CVD has been used for many years for a wide variety of deposits, and make it very attractive as a deposition technique.

Molecular-beam epitaxy (MBE) is a recent method of metal deposition. With this method, a beam of atoms of the desired deposit is directed at the wafer surface. The alignment of atoms into the proper crystal sequence is achieved by using low level incidence rates and by heating the wafer surface which aids migration. A super clean environment and substrate surface under high vacuum are a must in order to minimize contamination that would interfere with proper crystal structure formation at the metal-semiconductor interface.

Annealing is often not needed to obtain rectifying MS contacts with SiC. It is mainly used to obtain ohmic contacts with low contact resistivity and good thermal stability. When done, even at elevated temperatures, annealing contacts with SiC takes longer than with other semiconductors because of its low chemical reactivity. Thus rapid thermal annealing with SiC ohmic contacts usually can not be performed with good results. Annealing is usually performed in an argon or forming gas (3% H_2 in N_2) atmosphere. Annealing temperatures range from 300 to 1200 °C, and annealing times range from seconds to hours depending on the contact and characteristics desired.

Annealing often produces silicides and carbides at the interface between the metal and SiC which can change the size of the Schottky barrier and the contact resistance.

As mentioned, most metals form rectifying contacts with SiC in the as-deposited condition. The best SiC Schottky contacts are those with a large barrier height. Research has indicated that different processing methods affect whether a contact's barrier height will follow the Schottky limit or the Bardeen limit. Under the Schottky model, the metals must then posses large work functions if used with n-type SiC, and small work functions if used with p-type SiC. In order to be used in high temperature/high power devices, the Schottky contact must exhibit large breakdown voltages and good rectifying behavior at high temperatures. However, studies have shown breakdown voltages decrease and rectifying behavior changes to ohmic behavior with an increase in temperature.

As discussed in Chapter one, Table II lists recent studies of SiC Schottky diodes. J.R. Waldrop et al. performed many of the studies (12; 14; 45) listed, and one of the results of their work with n-type 6H-SiC was that the barrier height depended upon which crystal face the metal was deposited on. They found that the carbon (C) face was significantly more reactive than the Si-face. Other contact studies by S. Yoshida et al. (46) found that Au contacts still behaved well when annealed at 300 °C for one hour in Ar and at 500 °C for 90 minutes, but degraded into an ohmic contact when annealed at 700 °C. This dependence of ohmic and rectifying behavior on annealing temperature was also shown by H. Daimon et al. (47), who reported that Al contacts on n-type 3C-SiC showed ohmic behavior up to 400 °C, but switched to rectifying behavior when annealed at 900 °C, while the opposite was shown when a p-type SiC substrate was used instead. Ni

contacts on 3C-SiC were also shown to change from rectifying to ohmic behavior when annealed at 800 °C by A.J. Steckl et al. (48; 49). This was attributed to the formation of Ni silicides, which was confirmed by x-ray diffraction and Auger analysis.

High voltage 4H-SiC Schottky contacts with breakdown voltages of up to 1000V were reported by R. Raghunathan et al. (16), and up to 800 V by A. Itoh et al. (15) The groups obtained good Schottky contacts with Au, Ni, Ti, and Al.

3.5 Samples Used for This Study

The samples used for this study were made by the University of Cincinnati and an outside contractor. The Ni/6H-SiC Schottky barrier diode samples were made by A.J. Steckl et al. of the University of Cincinnati (50). The samples were fabricated upon a commercially available, lightly doped n-type 6H-SiC epitaxial layer grown on a more heavily doped n-type Si-face (0001) 6H-SiC substrate. The device structure is shown in Figure 11.
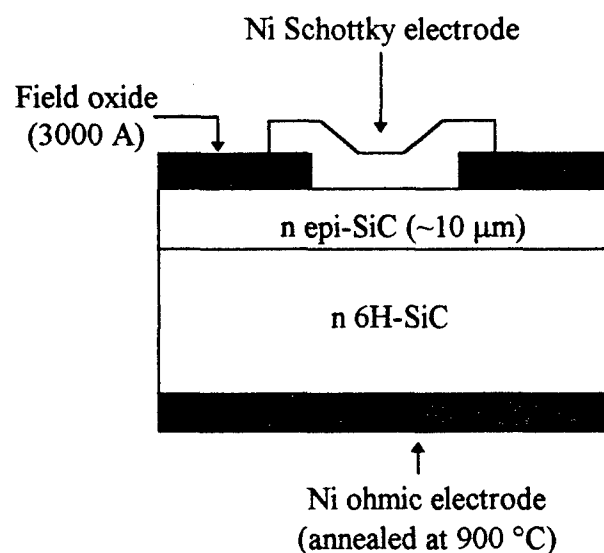

Figure 11. A schematic of a vertical structure Ni/6H-SiC Schottky diode (50).

The fabrication began with a wet thermal oxidation of the 6H-SiC at 1150 °C after chemical degreasing and standard RCA cleaning of the SiC sample. The thermal oxidation produces a ~ 600 angstroms oxide layer on the SiC epi-layer. To provide a low contact resistance ohmic electrode, a layer of Ni was sputter-deposited on the cleaned backside surface. The sputtering was followed by a 5-minute anneal at 900 °C in an Ar atmosphere. This formed a good ohmic contact made of a Ni-silicide layer on the SiC substrate. An additional oxide layer (~ 2500 angstroms) is then sputter-deposited onto the thermally grown layer on the SiC epi-layer. The field oxide is thus brought to a total thickness of ~ 3000 angstroms. A contact window is etched in the oxidized SiC epi-layer, and then Ni is sputter deposited through the window. This forms the active Ni-SiC rectifying electrode. The Ni depositions were done with a sample stage at 135 °C. Ni films of 4000 angtroms thickness were deposited at a rate of 200 angstroms per minute, using RF power at 250 W with a chamber pressure of 5 millitorr. The circular Ni rectifying electrode was patterned by chemical etching, and the edge of the electrode overlapped the field oxide. The process produced devices of 140-160 μm in diameter. A sample section of the wafer containing 38 devices was obtained.

The outside contractor's Pt/4H-SiC Schottky diodes were made upon an epi-layer grown in two doping runs on a more heavily doped n-type C-face (000-1) 4H-SiC substrate. The epilayer was grown in two 4.5 μm thick runs. The first layer was doped about $N_D = 1.5 \times 10^{16}$ cm^{-3}, and the second layer (the one closest to the MS interface) was doped about $N_D = 4 \times 10^{16}$ cm^{-3}. The platinum was deposited by evaporation onto the wafer surface. The wafer was then diced producing several hundred individual devices of the

49

same diameter. Reverse current tests were performed using a Keithley 236 Source Measure Unit to screen for the devices with the least reverse current at a nominal (-30V) bias. Twenty-four Pt/4H-SiC devices along with the thirty-eight Ni/6H-SiC devices were chosen and were sent to Wright-Laboratories' Solid State Electronics lab for packaging.

As shown in Figure 12, The packaging consisted of a gold-plated metal frame wrapped in ceramic. The interior chamber was circular and allowed for 42 connections. These interior connections corresponded to 42 outside pins on the package. The base of the interior chamber was the gold-plated metal. The samples were mounted on the base of the interior with adhesive, and wires were attached to the connectors to the outside pins. Four interior pins were connected to the base directly to enable exterior pins to act as ground (the frame was ground as well). The packaging enabled quicker testing of the diodes, and allowed for further screening of devices. Devices were chosen on their ability to give good results for temperatures up to 698 K without any breakdown occurring. For this research, two Pt/4H-SiC and three Ni/6H-SiC Schottky diodes were tested and analyzed using I-V-T, C-V-T, C-f-T, and DLTS techniques. The diameters of the two Pt/4H-SiC Schottky diodes were 336 μm, while for the Ni/6H-SiC samples, the diameters were 141, 151, and 160 μm.
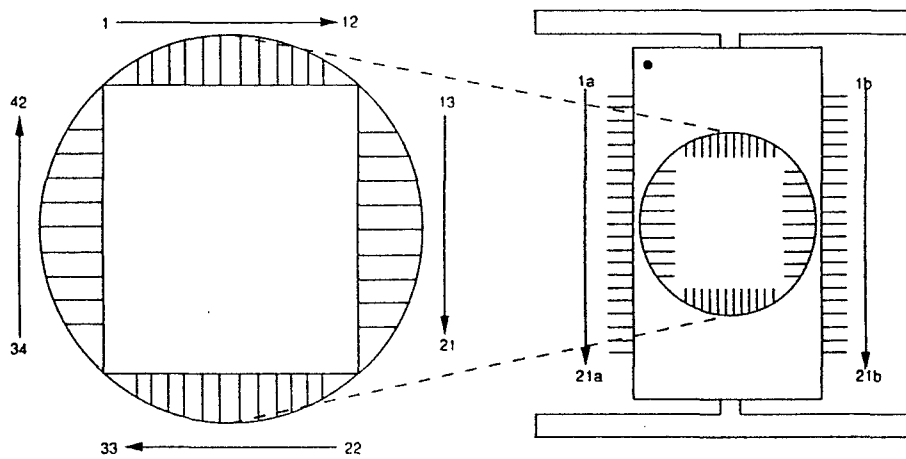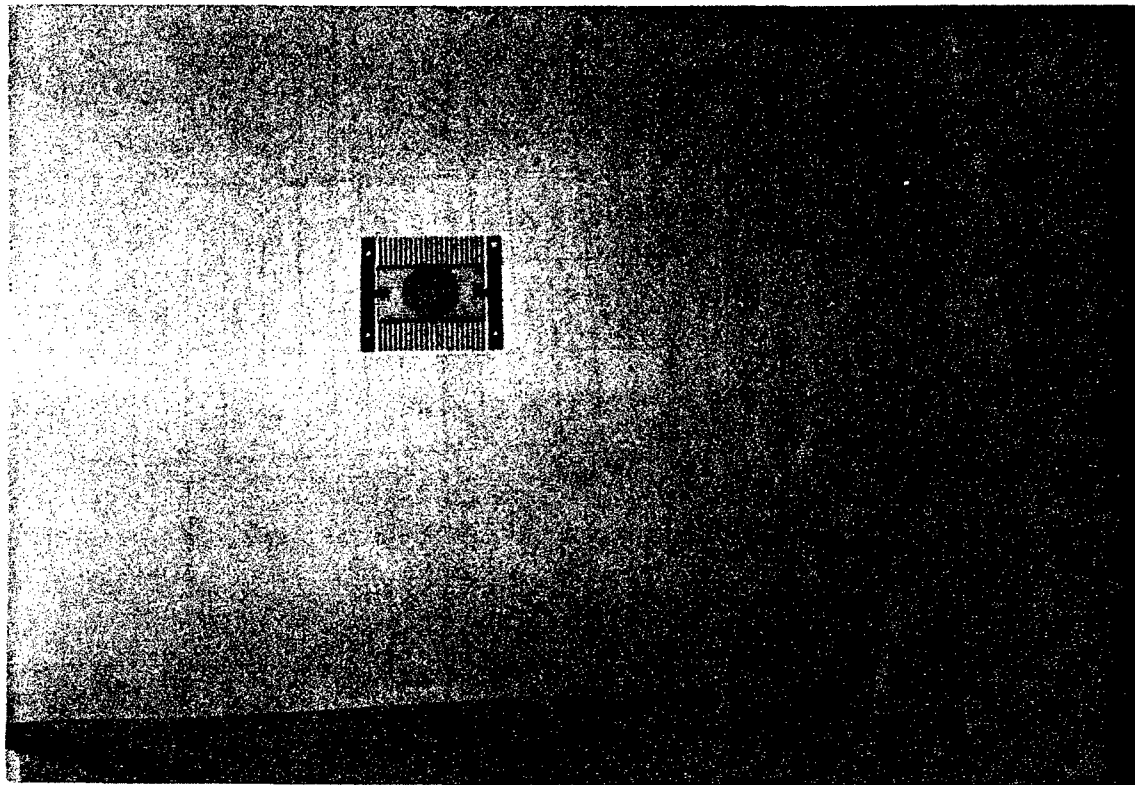
Figure 12. Photograph and diagram of packaging used for 4H- and 6H-SiC Schottky diode samples.

4. Theory and Procedures of Experiments

4.1 Current-Voltage-Temperature

Forward and reverse current-voltage tests at various temperatures allow for quantitative determination of Schottky barrier height, the ideality factor, the effective area-Richardson's constant product, series resistance, and activation energies. Also, qualitative analysis of current characteristics can be made to determine the effects of the different current transport processes in the device.

Forward current-voltage-temperature tests begin by assuming that thermionic-diffusion currents are predominant, but that there are tunneling currents present. Equation (3.41) is used, adding in the ideality factor, n, as in equation (3.43). This gives an equation that accounts for quantum-mechanical effects, tunneling, and recombination currents along with the thermionic-diffusion currents. By taking the natural logarithm of the forward current, one can determine the ideality factor n from the linear portion of the curve. The intercept of that will also give the saturation current, I_S. By taking forward current-voltage plots at different temperatures, a plot of $Ln(I_S/T^2)$ vs. $1000/T$ will then yield the barrier height and the active area-effective Richardson's constant product, from the relations:

$$I_S = AA**T^2 \exp(-\frac{q\phi_{Bn}}{kT}) \qquad (4.1a)$$

$$Ln(\frac{I_S}{T^2}) = Ln(AA**) - \frac{q\phi_{Bn}}{kT}. \qquad (4.1b)$$

Thus the slope will yield the barrier height, and the intercept will yield the active area-effective Richardson's constant product. The series resistance can be determined by measuring the slope of the current versus high voltage.

Reverse current includes effects from Schottky barrier lowering, thermally generated space-charges, a voltage-independent bulk diffusion component, and edge leakage currents (33:90). For most practical Schottky devices, edge leakage currents are the major current component. However, for wide band-gap semiconductors, the reverse current contains a substantial generation component as well, because of the small majority carrier concentration. Neglecting the Schottky barrier lowering, bulk and edge leakage components of the reverse current I_{rev} can be written as (51:147):

$$I_{rev} \approx I_{gen} \approx \frac{qAn_eW}{\tau_g} \propto \exp(\frac{-E_g}{2kT}), \qquad (4.2)$$

where τ_g is the generation lifetime. τ_g is given by:

$$\tau_g = \tau_p \exp\left[\frac{(E_t - E_i)}{kT}\right] + \tau_n \exp\left[\frac{-(E_t - E_i)}{kT}\right], \qquad (4.3)$$

where τ_p and τ_n are the lifetimes of the holes and electrons in the generation/recombination center at energy E_t, respectively. E_i is the intrinsic Fermi level. Combining (4.2) and (4.3) yields:

$$I_{rev} \propto \exp(\frac{-E_a}{kT}), \qquad (4.4)$$

where

$$E_a = E_c - E_t \text{ for } E_t > E_i \qquad (4.5)$$

53

and

$$E_a = E_t - E_c \text{ for } E_t < E_i. \tag{4.6}$$

Here E_a is the activation energy of the generation/recombination center.

For two generation/recombination centers, equation (4.4) can be written as:

$$I_{rev} = C_1 \exp(\frac{-E_{a1}}{kT}) + C_2 \exp(\frac{-E_{a2}}{kT}), \tag{4.7}$$

where C_1 and C_2 are proportionality constants. Thus, taking the natural logarithm of the reverse current versus $1/kT$ for a given reverse bias will yield a linear portion for each activation energy. From the slopes of these linear portions, the activation energy is found.

Low temperature current studies were done at the Air Force Institute of Technology using the apparatus shown in Figures 13 and 14. A Janis coldhead was used to enclose the sample package in a vacuum of 1 microtorr. The samples were cooled to 100 K with a closed cycle nitrogen refrigerator. The current tests were done with a Keithley 238 source measure unit. The unit was IEEE interfaced with a computer which controlled and acquired the data. The current tests for each sample were done in two runs. The first went from -100 to 0 V in one volt steps, the second went from 0 to 2.0 V in 0.02 V steps. The current data was taken from 100 K to 300 K in 20 K intervals using a Lakeshore 330 Autotuning temperature controller.

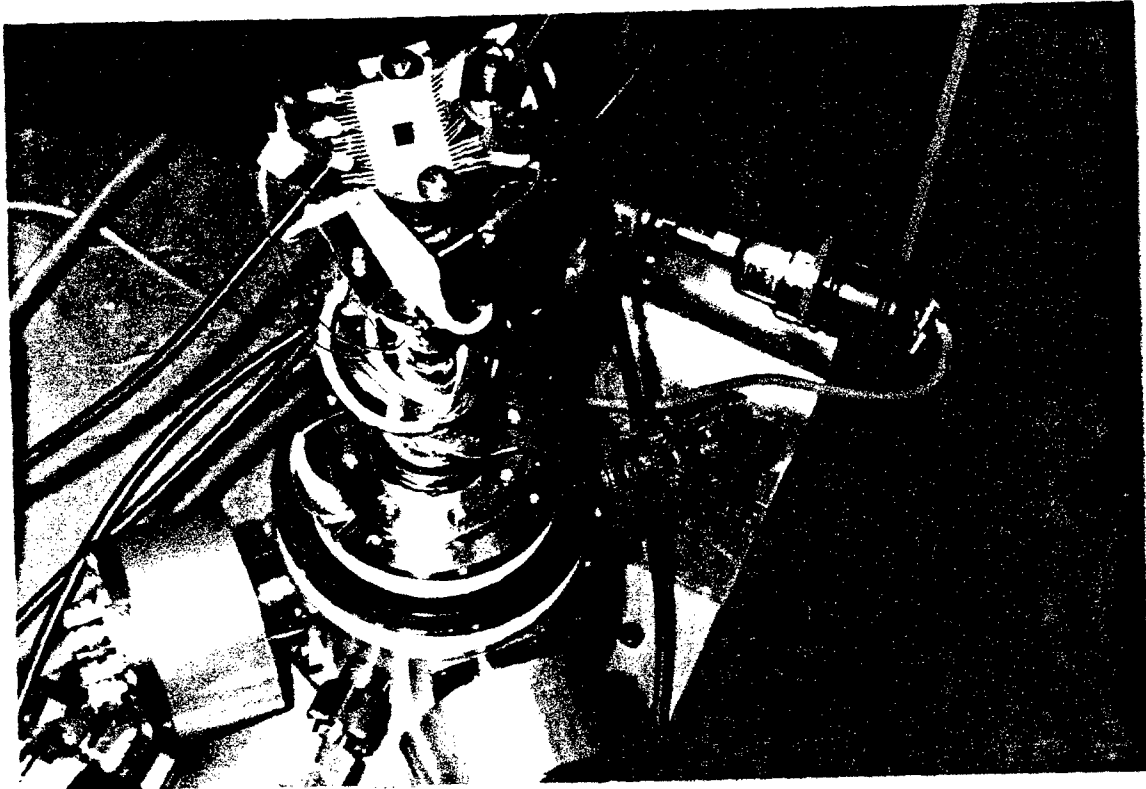Figure 13. Photograph of low temperature set up for I-V-T and C-V-T measurements.

Figure 14. Photograph of mounted sample in low temperature set up for I-V-T and C-V-T measurements.

High temperature current data was acquired at Wright-Laboratories' Power Semiconductor branch of the Power and Propulsion directorate. The samples were placed in a large steel vacuum chamber on a copper block which was on top of a ceramic block. The copper block contained a temperature sensor in the middle and acted as the sensor for the sample temperature. The ceramic block was heated by a Microscience Heater Control HPC 1000. The sample's package was connected by alligator clips to ceramic covered wires, which were attached to pins that led outside the chamber. The chamber was pumped down to under 1×10^{-7} torr (see figure 15 and 16). The samples were heated from 295 to 348 K, then from 348 to 648 K in 50 K increments. Current tests were done using a Keithley 236 Source Measure Unit. The current tests were conducted at the same voltage range and steps as for the low temperature measurements. Because they are two different systems, the low temperature and high temperature data are analyzed separately.

4.2 Capacitance-Voltage-Temperature and Capacitance-Frequency-Temperature

Reverse bias capacitance-voltage-temperature tests can yield the Schottky barrier height and the carrier concentration of the device. From equation (3.23), the inverse of the capacitance squared is:

$$\frac{1}{(CA)^2} \equiv \frac{2(\phi_B - V_n - V - \frac{kT}{q})}{A^2 q \varepsilon_S n_e}. \tag{4.8}$$
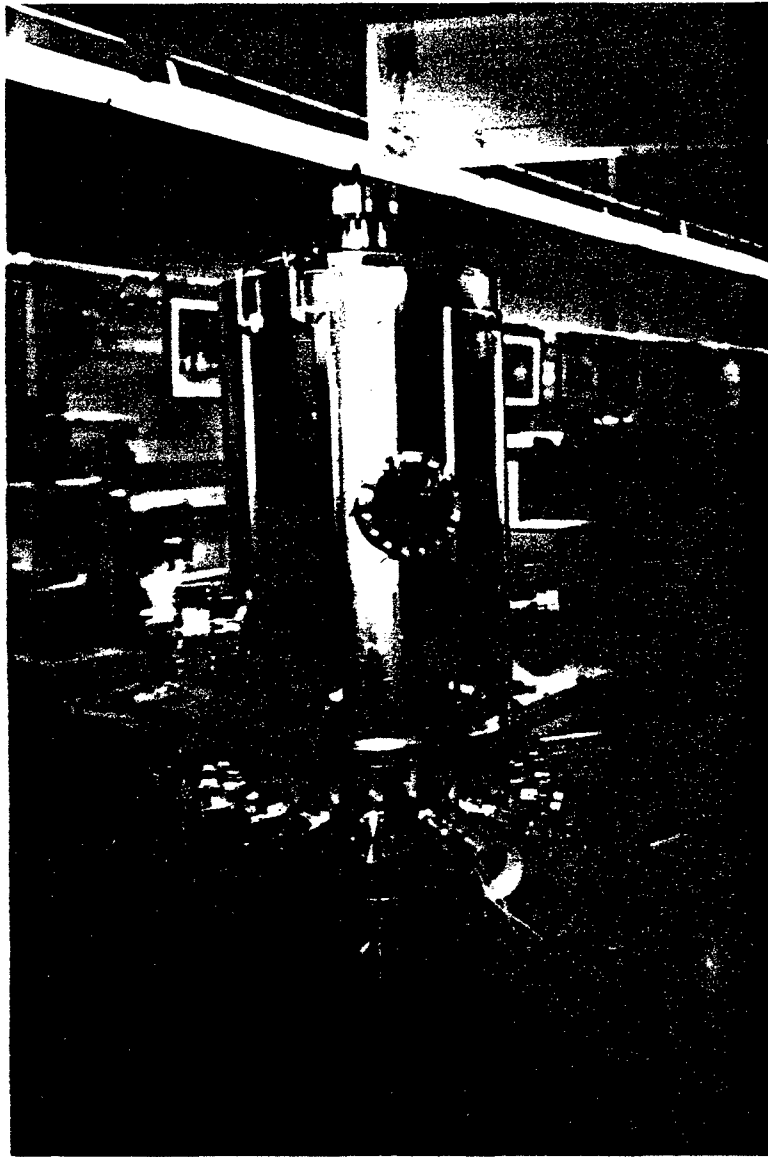
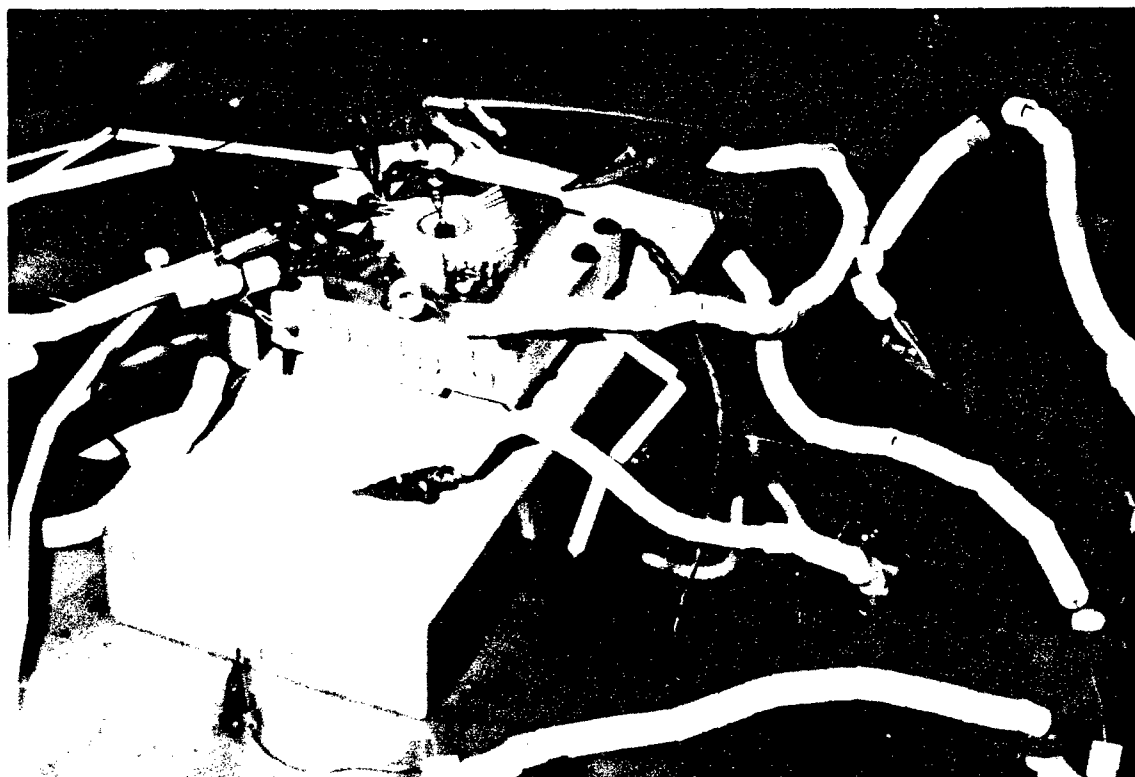Figure 15. Photograph of high temperature vacuum chamber for I-V-T and C-V-T measurements.

Figure 16. Photograph of mounted sample in high temperature setup for I-V-T and C-V-T measurements.

Taking the derivative with respect to voltage yields:

$$-\frac{d(1/(CA)^2)}{dV} = \frac{2}{A^2 q \varepsilon_S n_e} .$$

(4.9)

Thus a plot of the inverse-squared of capacitance versus voltage yields the carrier concentration from the slope as shown by:

$$n_e = \frac{2}{q \varepsilon_s} \left[\frac{-1}{\frac{d(1/(CA)^2}{dV}} \right] .$$

(4.10)

The intercept on the voltage axis, V_i, yields the unlowered barrier height,

$$\phi_B = V_i + V_n + \frac{kT}{q} .$$

(4.11)

The curve will not usually be linear for large ranges of reverse bias. This occurs because as the reverse voltage increases, the depletion width widens as $\sim (V)^{1/2}$. More carriers are thus included in the depletion region. Surface defects, edge leakage currents, and deep level impurities can also contribute carriers to the depletion region. Capacitance measurements are very sensitive to carrier concentration, therefore at higher voltages the signal will be noisier.

Although dependent on voltage, the slope of the capacitance-voltage relationship is generally insensitive to temperature. This is because the field-ionized impurity concentration is being measured, not the thermally ionized carrier concentration in the semiconductor bulk. Also, at low enough temperatures, freeze out can occur in which

case the depletion width approaches the thickness of the bulk substrate, and the electric field is reduced to below the ionization limit (32). The capacitance-voltage measurements were made by putting a negative bias DC signal through the device on which an AC signal is superimposed. The DC signal creates the depletion width, while the AC signal varies the width by small amounts at the frequency of the signal. The capacitance for different frequencies will vary depending upon the emission/capture rates of the carriers. If the AC signal is at too high of a frequency the carriers with a low emission/capture rate will not be swept into the depletion region. This leads to the next type of test, capacitance-frequency-temperature.

As mentioned, by studying the capacitance at different frequencies, the emission/capture rates can be determined. This technique depends upon the oscillating voltage which will cause captured carriers to be emitted and then recaptured. If capture and emission rates are both larger than the frequency of oscillation, then a steady-state capacitance will result. However, as previously stated, if the rates are too low, they will not be able to respond to the oscillating voltage, and the measured capacitance will be less. Since the emission rates depend upon temperature as $e_p \propto \exp(-E_a/kT)$ (52), by studying the capacitance versus frequency data for different temperatures, the temperature at which the emission rate equals the oscillation frequency can be determined. The activation energy of the trap, E_a, can then be determined from two temperatures, T_1 and T_2, at which the emission rates equals two different frequencies, f_1 and f_2 (53: 28).

$$E_a = E_t - E_a = \frac{kT_1T_2}{T_2 - T_1}\left[\exp(\frac{f_1}{f_2}) - 2\ln(\frac{T_2}{T_1})\right]. \qquad (4.12)$$

T_1 and T_2 can be determined from a plot of dC/dT versus temperature. At the maximum rate of change in capacitance, the trap begins to follow the oscillating voltage. The temperatures at which this occurs will correspond to peaks on the plot.

The capacitance tests were conducted in the same setup as for the current tests. The voltage range and steps differed, however. A Keithley 590 CV analyzer was used to test the capacitance from 0 to -19.5 V in -1.95 V steps. The tests were done at 100 KHz and 1 MHz. To minimize noise from current entering the ceramic block, it was necessary to turn off all peripheral equipment such as the heater, the temperature sensor, etc.

4.3 Deep Level Transient Spectroscopy

Deep level transient spectroscopy (DLTS) allows for a fast thermal scan of deep centers that are electrically active within the depletion region. In DLTS, the MS contact capacitance transients are measured. These transients result from the filling and emptying of energy levels with free carriers as shown in Figure 17. The capacitance equation (3.23) at a given temperature can be rewritten to expand the concentration of electrons in the conduction band, n_c, into two parts, N_D^+ and $N_t\exp(-t/\tau)$, as shown in (54):

$$C(t) = \sqrt{\frac{q\varepsilon_S(N_D^+ - N_t \exp(-t/\tau))}{2(\phi_B - V_n - V - \frac{kT}{q})}}, \qquad (4.13)$$

where N_D^+ is the concentration of ionized donors, N_t is the concentration of electron traps times, and τ is the lifetime of the trap.
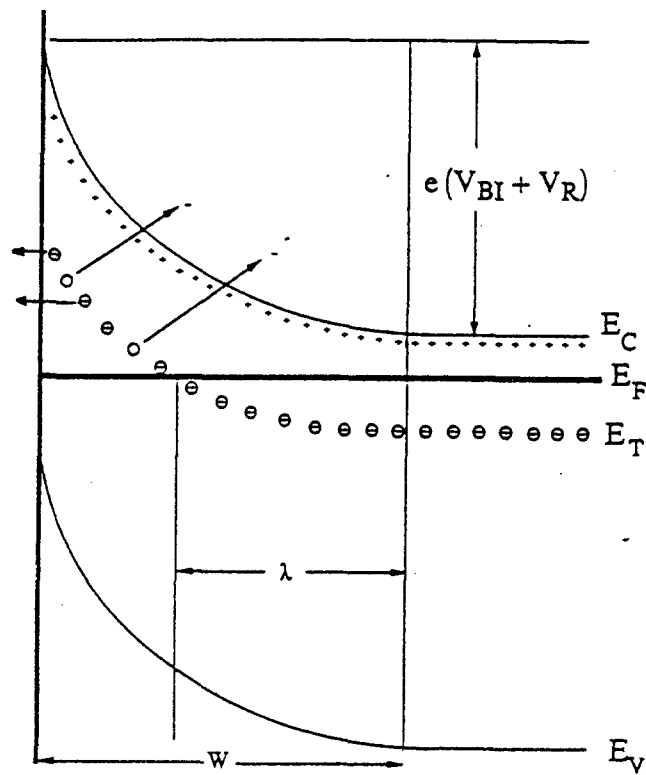
Figure 17. Diagram of a Schottky diode with traps. Emitted carriers can tunnel through the barrier or be thermally excited.

63

The square of the capacitance thus decays exponentially to an infinite, quiescent time value given by:

$$C^2(t) = C^2(\infty) - \frac{N_t}{N_D^+}\exp(-\frac{t}{\tau})C^2(\infty).$$

(4.14)

For the usual case, where $N_D^+ \gg N_t$, the capacitance can be simplified using binomial expansion such that:

$$C(t) = C(\infty) - \frac{N_t}{2N_D^+}\exp(-\frac{t}{\tau})C(\infty).$$

(4.15)

Fitting the capacitance transients to an exponential decay allows one to calculate the trap concentration and emission rates at a fixed temperature. The emission rate of a trap depends upon temperature as:

$$e_n = \frac{\sigma_n \langle v_n \rangle N_c}{g}\exp(-\frac{E_a}{kT}),$$

(4.16)

where σ_n is the capture cross section of the trap, g is the degeneracy of the deep state, and $\langle v_n \rangle$ is the mean velocity. Including the temperature dependence of N_C ($\sim T^{3/2}$) and the mean velocity ($\sim T^{1/2}$), and grouping the rest of the constants into a proportionality term, $\sigma(\infty)$, yields:

$$\frac{e_p}{T^2} = \sigma(\infty)\exp\left(-\frac{E_a}{kT}\right).$$

(4.17)

Therefore, by obtaining the emission rates at many different temperatures, the activation energy of a trap can be found from the linear slope of $\mathrm{Ln}(e_p/T^2)$ vs. $1/kT$. The above plotting process is called an Arrhenius analysis.

The DLTS measurements were performed at the Air Force Institute of Technology at the same station as the low temperature studies as shown in Figure 13. The test runs were done from 100 to 600 K in 4 K increments. A diagram of the DLTS setup is shown in Figure 18.
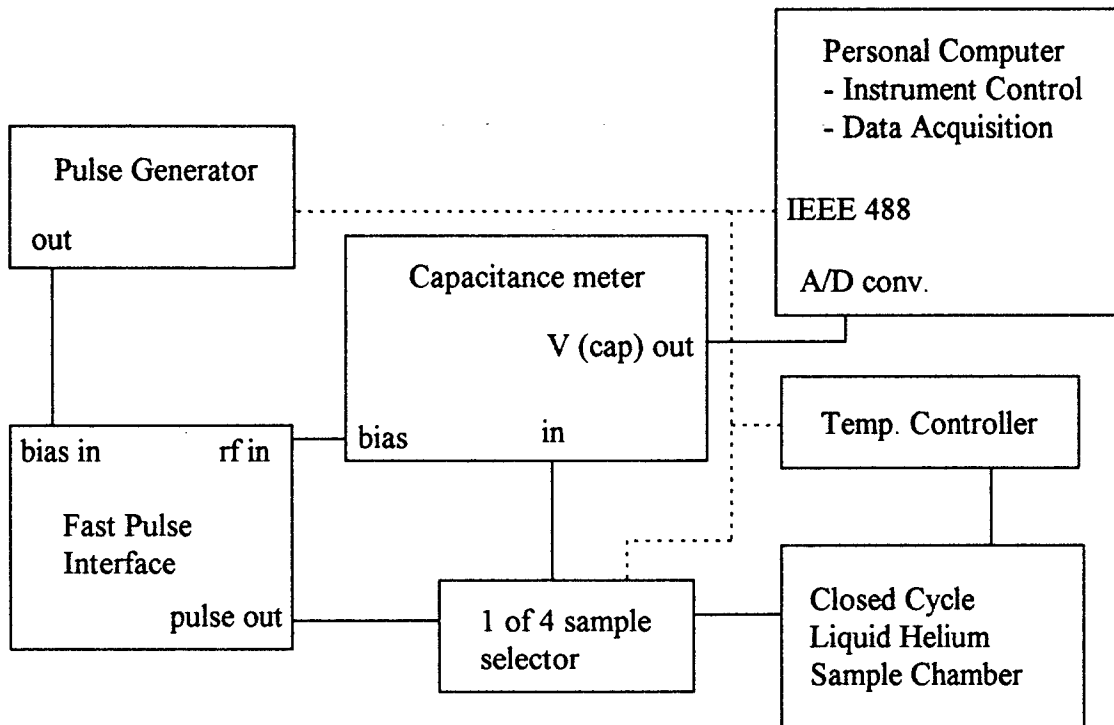

Figure 18. Schematic diagram of DLTS system. Solid lines are input/output paths for the DLTS equipment. Dashed lines are IEEE 488 bus control lines.

4.4 Breakdown Voltage Tests

Investigation into the effects of edge leakage currents was performed using Fluorinert brand non-reacting electrical solvent. The Fluorinert is non-reactive and non-conductive liquid and removes the edge leakage paths by removing ionic charges on the surface and edges of the device. These ionic charges on the surface induce image charges in the semiconductor thus creating surface channels. Breakdown studies were conducted using a Tektronix 370A programmable curve tracer at room temperature. The samples were mounted in the high temperature chamber to enable a good ground.

5. Results and Analysis

5.1 Current-Voltage-Temperature (I-V-T)

Forward current-voltage tests revealed many interesting aspects. Some of the diodes tested behaved very well exhibiting linear I-V characteristics as described by thermionic emission theory. However, others exhibited large tunneling components which distorted the linear behavior by bulging the curves at lower forward bias. A typical forward voltage comparison between a well-behaved 6H-SiC Schottky diode and a 6H-SiC Schottky diode with a large tunneling component is shown in Figure 19. What was seen was that the well-behaved Schottky diodes had a very linear portion, showing dominance by thermionic emission currents. However, diodes that had large tunneling current components exhibited a bulge in the curve. Figures 20 and 21 show the current-voltage curves at different temperatures for the well-behaved Ni/6H-SiC Schottky diodes. The diodes were found to perform well even at nearly 700 K. The I-V curves for the Ni/6H-SiC Schottky diode with the larger tunneling component is shown in Figure 22. It is notable that as the temperature is increased, the bulge in the current slope due to tunneling decreases. This is in agreement with theory as represented by the kT/E_{00} ratio. Theory predicts that at higher temperatures the thermal emission of electrons over the barrier increases to the point that it dominates the tunneling currents which stay relatively constant versus temperature.
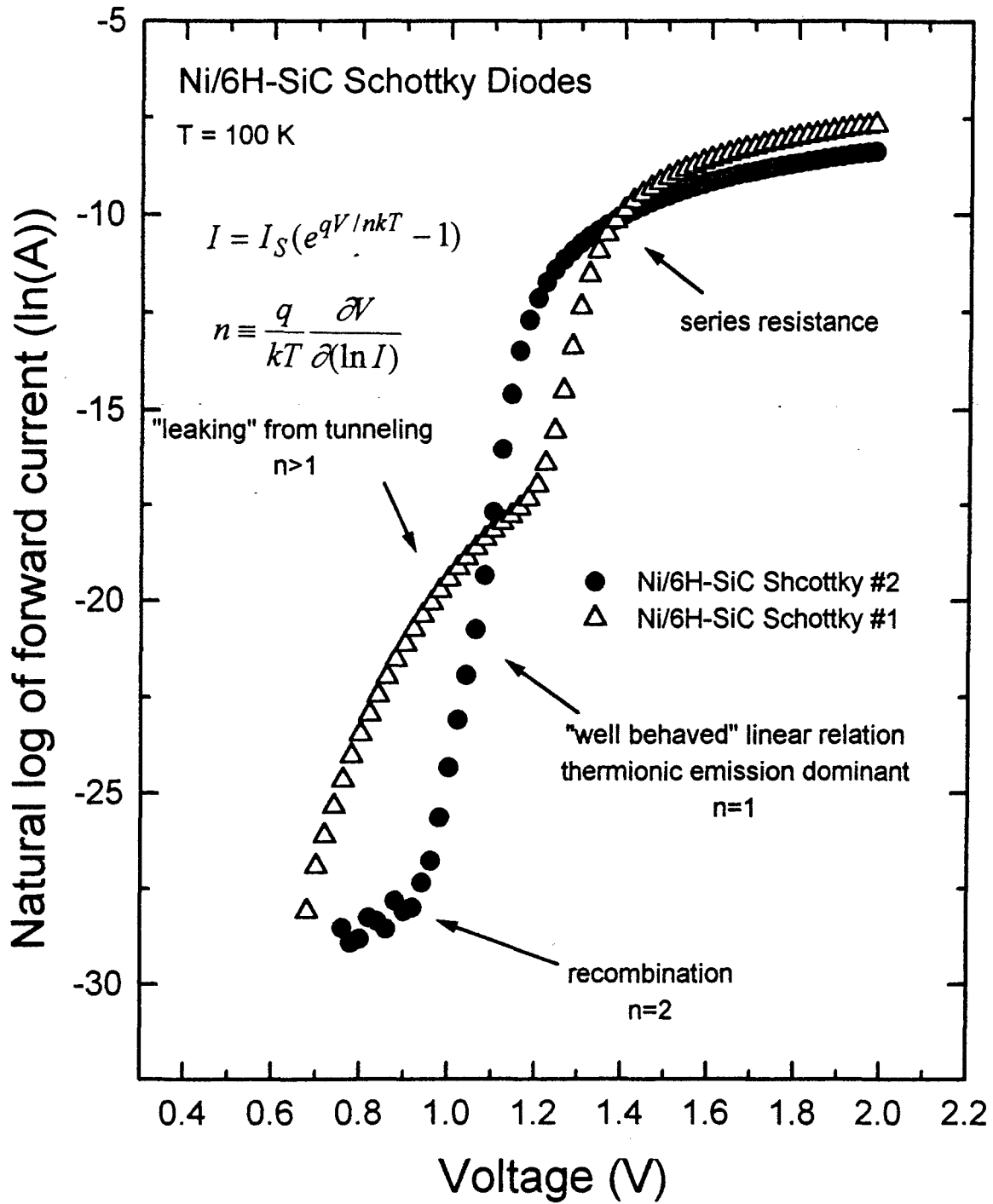
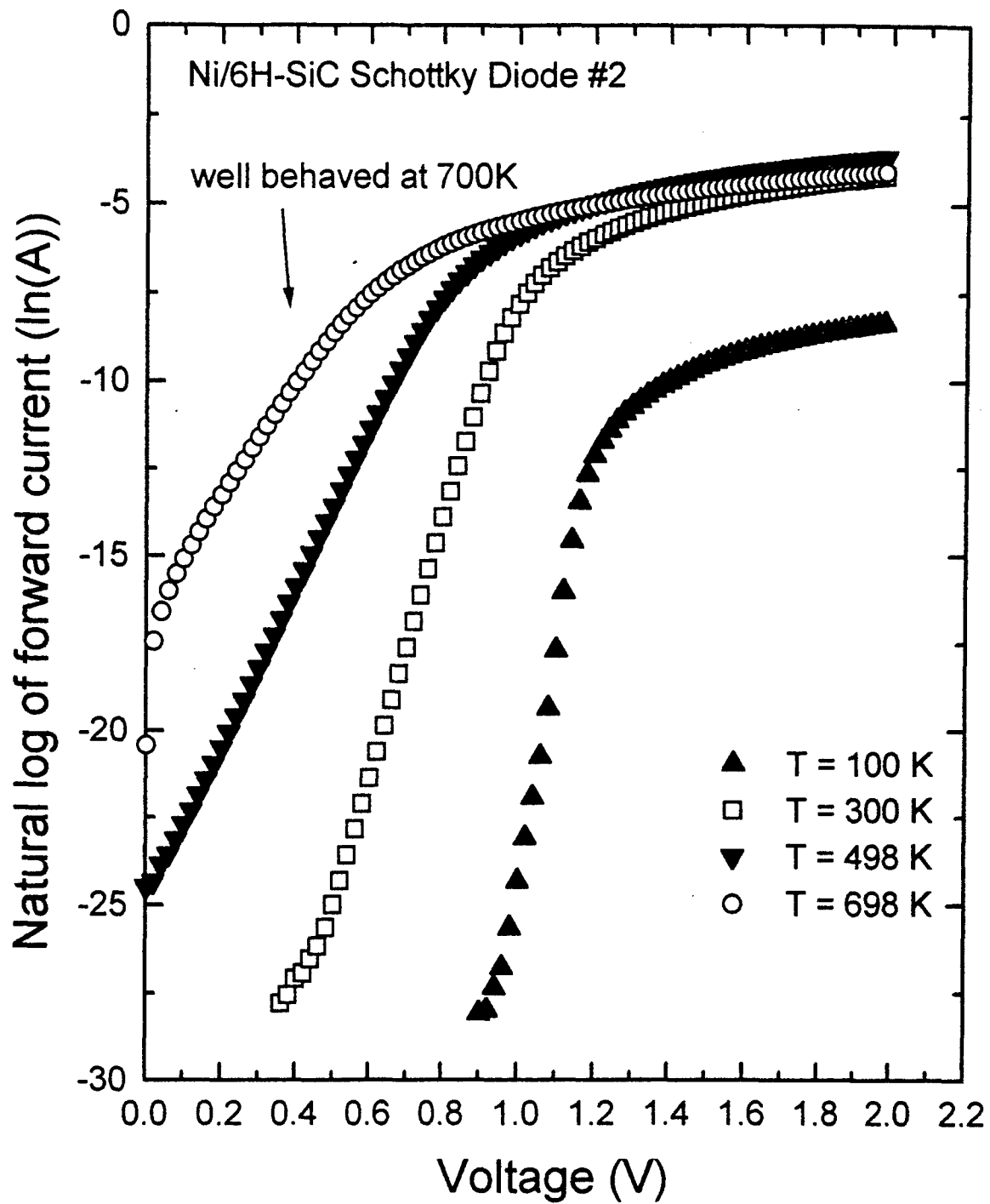Figure 19. Current-voltage curve of two Ni/6H-SiC Schottky diodes illustrating the effect of tunneling.

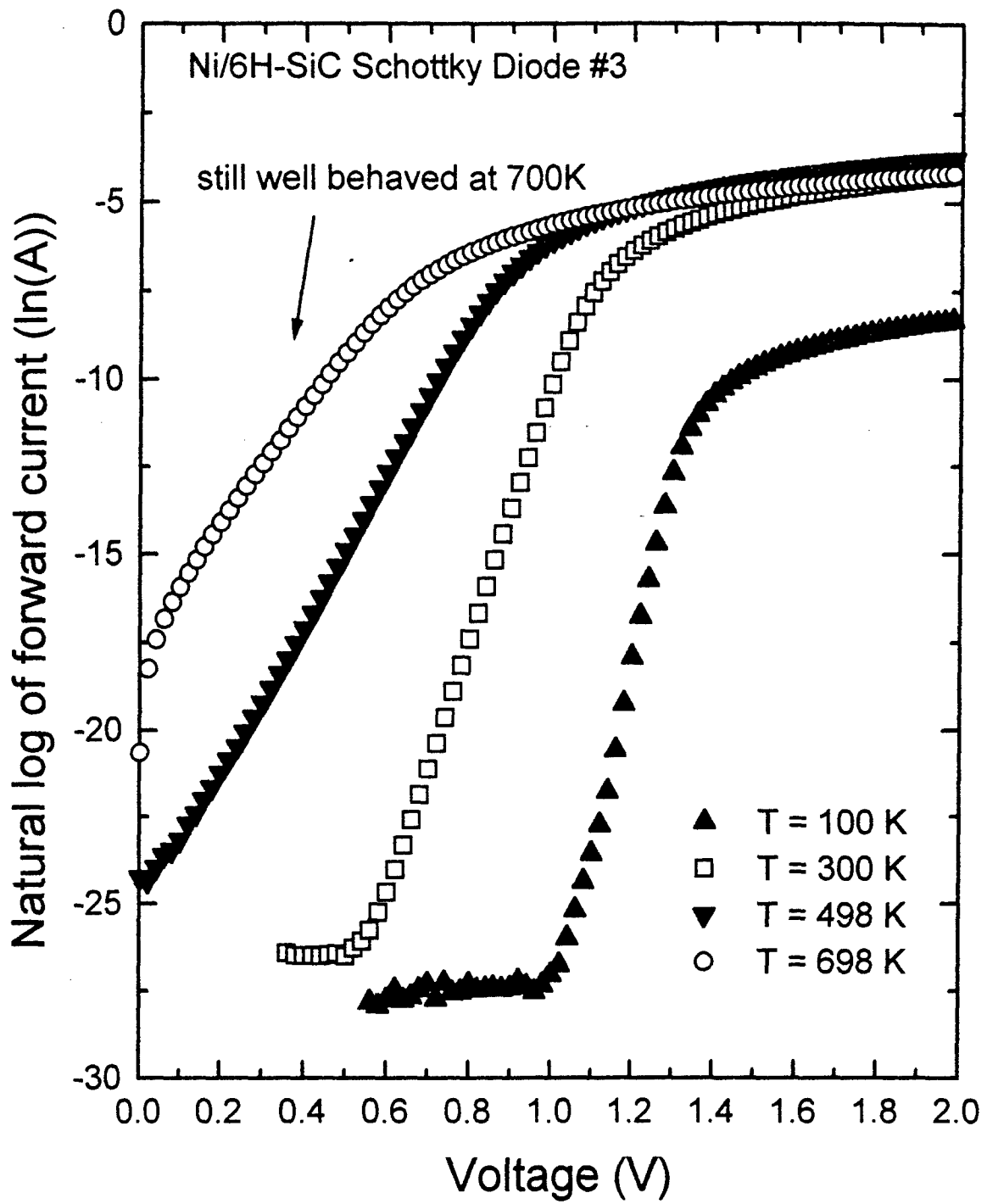Figure 20. Current-voltage curve of Ni/6H-SiC Schottky diode #2 at different temperatures.

69

Figure 21. Current-voltage curve of Ni/6H-SiC Schottky diode #3 at different temperatures.
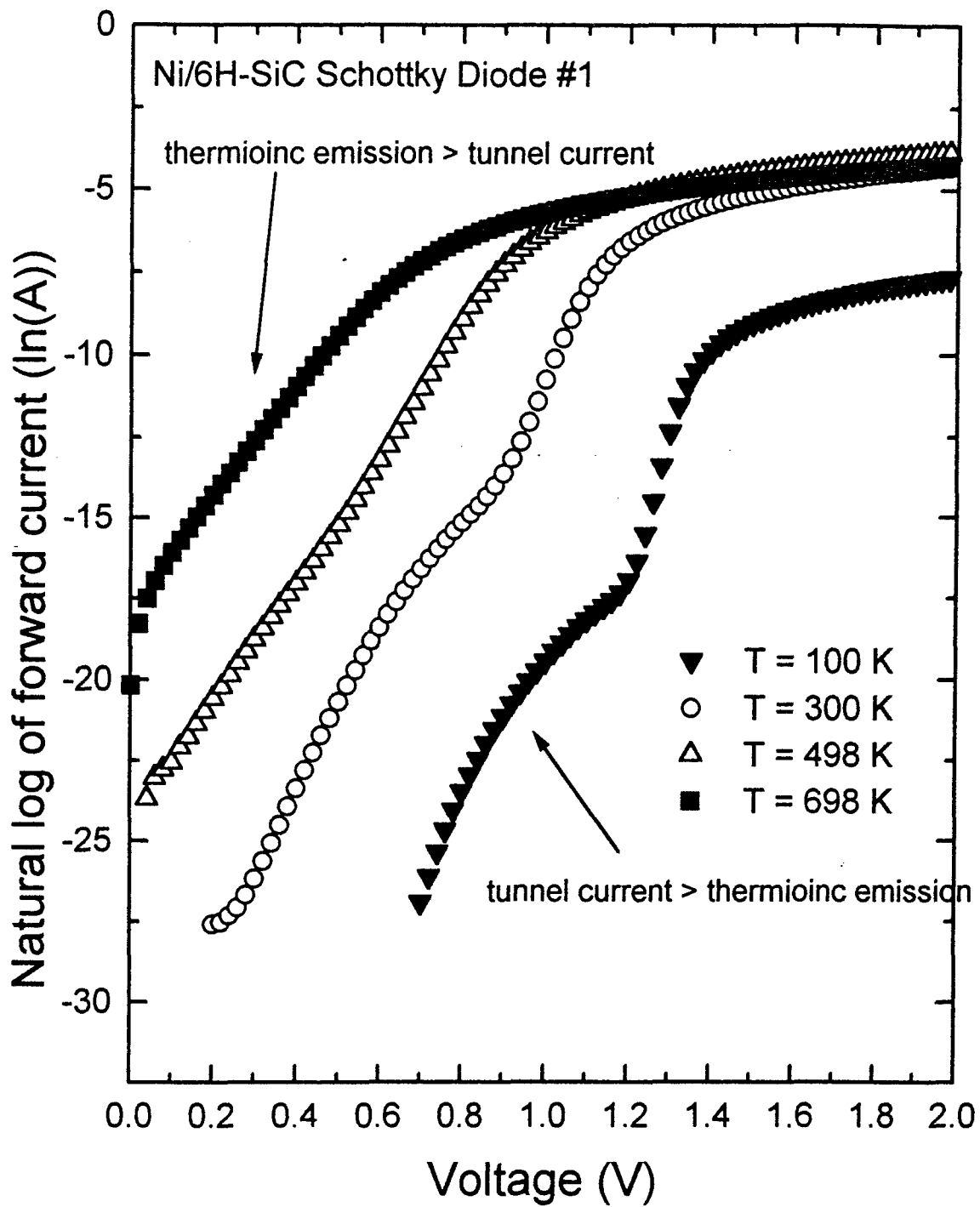
Figure 22. Current-voltage curve showing decrease in bulge in current at higher temperatures for Ni/6H-SiC Schottky diode #1.

71

The series resistance also played a large part in the behavior of the diodes, as can be seen in the rounding off of the linear slope at high voltages caused by the current limiting behavior of the resistance. In Figures 23 and 24, the Pt 4H-SiC Schottky diodes' high series resistance is shown at various temperatures. This high series resistance causes greater bending at high temperatures because the number of carriers in the conduction band is greater, and thus currents are greater. Since series resistance affects higher currents more than lower currents, the resistance affects the curves at lower voltages for the higher temperatures.

The plots show that the second 4H-SiC device, shown in Figure 24, has a large tunneling component as compared to the first 4H-SiC device, shown in Figure 23. All the curves exhibited linear behavior at some portion. Finding the slope, then using equation (3.44), the ideality factors were calculated to within an accuracy of ±0.05. The ideality factors of the 6H-SiC samples were found to decrease with temperature, approaching the ideal value of one (see figure 25). This reaffirmed the theory that thermionic emission currents dominate tunneling and recombination currents at higher temperatures. The factor of 2 in the denominator of the exponent term in equation (3.48) indicates that when recombination currents begin to dominate, the ideality factor will approach two. This occurs for Ni/6H-SiC Schottky diode #3 at low temperatures, as shown in Figure 25, and thus recombination currents are dominant. The ideality factor of Ni/6H-SiC diode #2 was seen not to increase beyond n=1.4. This indicates that the thermionic emission currents in this device are more dominant at low temperatures than they are in Ni/6H-SiC diodes #1 and #3.
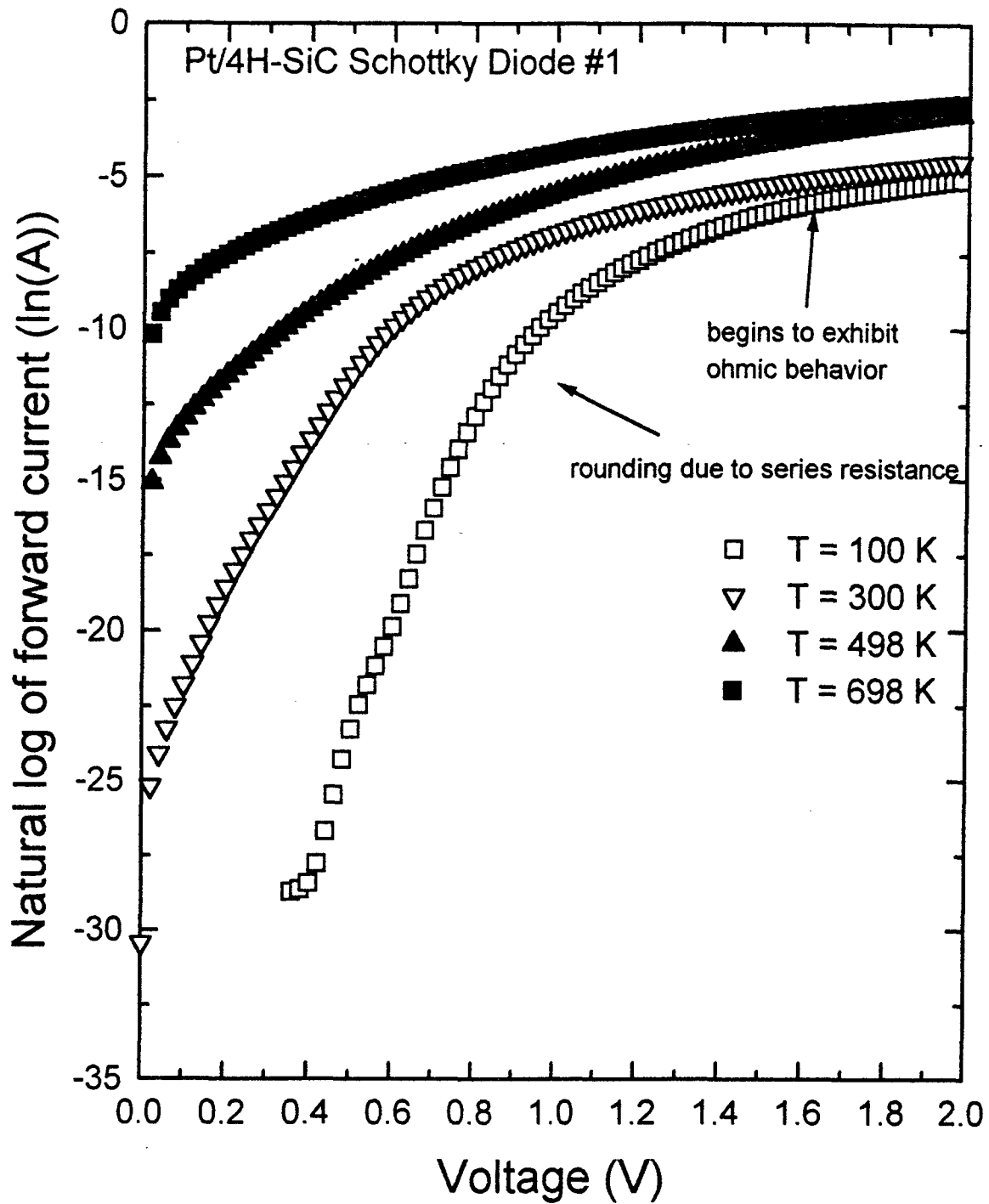
Figure 23. Current-voltage curve illustrating effect of series resistance at different temperatures for Pt/4H-SiC Schottky diode #1.
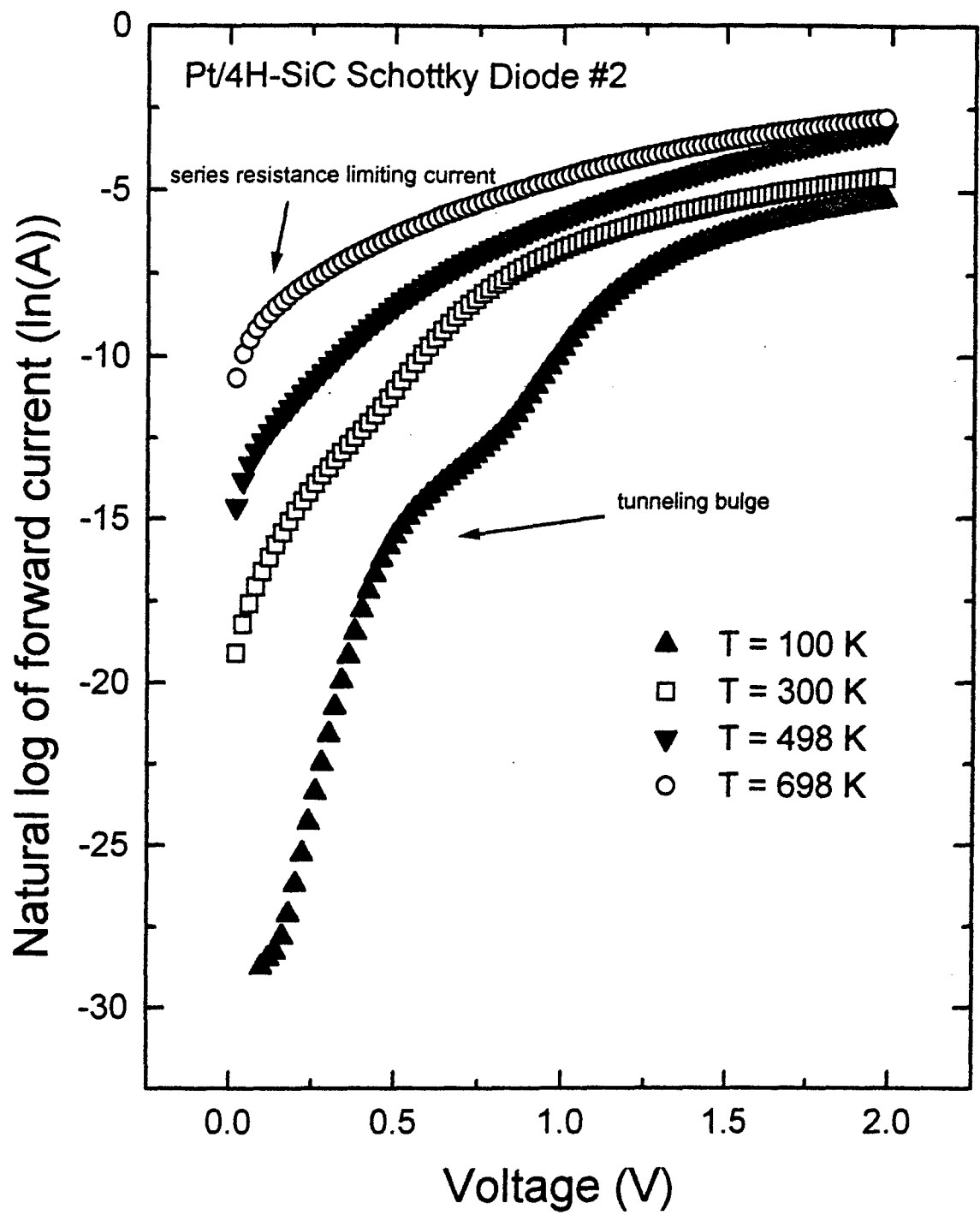
Figure 24. Current-voltage curve illustrating effect of series resistance at different temperatures for Pt/4H-SiC Schottky diode #2.
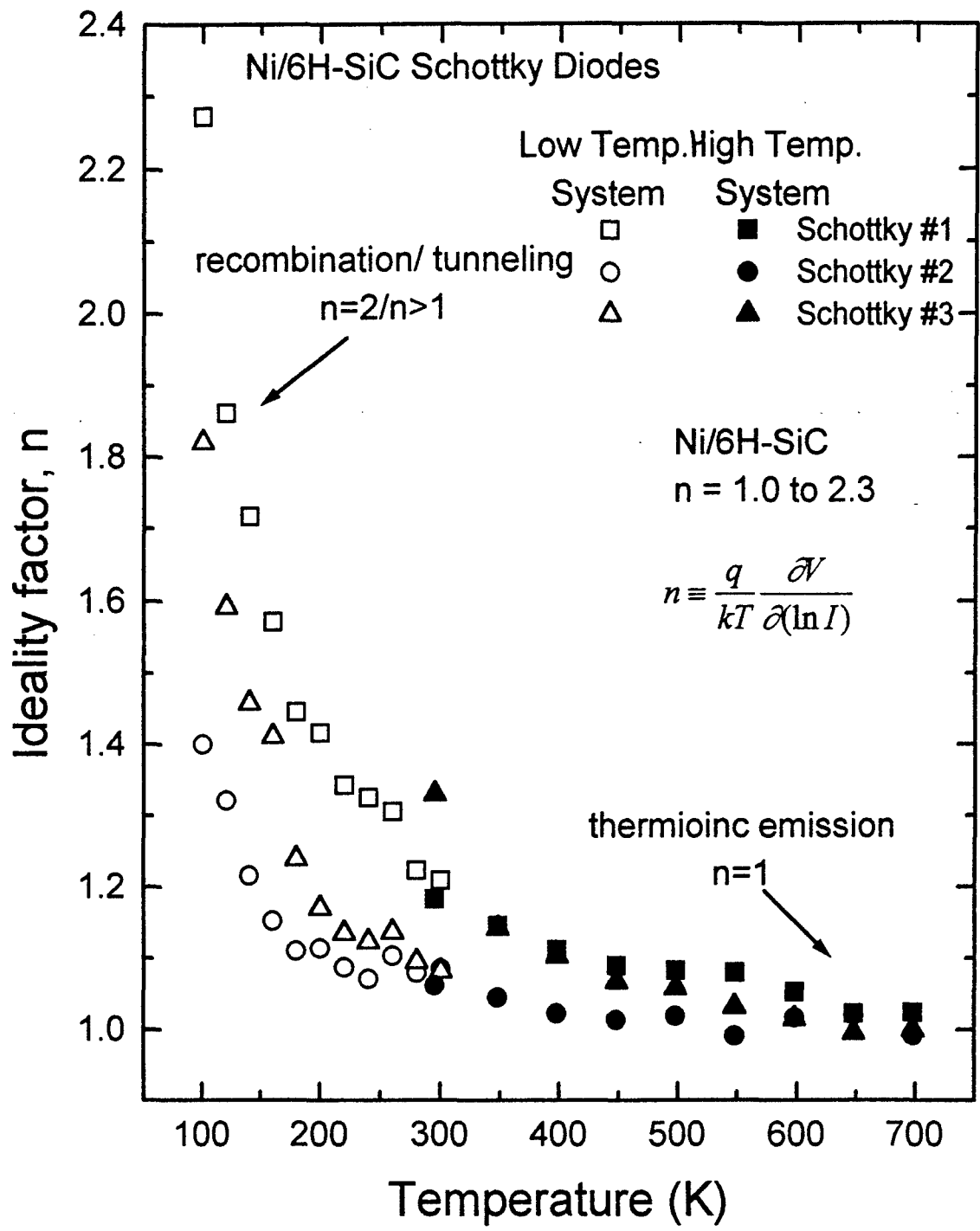
Figure 25. Plot of the ideality factor versus temperature for the Ni/6H-SiC Schottky diode samples.

The ideality factor of 6H-SiC diode #1 was seen to increase beyond two, indicating that tunneling is the dominant process at low temperatures.

Figure 26 shows a plot of the ideality factor for Pt/4H-SiC Schottky diode #1 as a function of temperature using data from both the low and high temperature system's current-voltage tests. The ideality factor, for the Pt/4H-SiC samples exhibited an interesting behavior. It decreased until 300 K, but then started to increase again (see Figure 26) at higher temperatures. The lowest ideality factor was about 1.6, increasing to nearly 3 at 100 K. This indicates that tunneling is a dominant process at low temperatures. On the other hand, the increase in the ideality factor to nearly three as the temperature increases is attributed to the effects of the series resistance on the current curve. As shown in Figures 23 and 24, the series resistance comes into play at smaller voltages for higher temperatures. This occurs because the temperature acts as a forward bias and shifts the current to encounter series resistance at less voltage. The slopes where the series resistance takes effect are flatter and the ideality factor is thus increased. This illustrates a breakdown in the theoretical basis for the ideality factor which is based upon the slopes of the linear region of the current-voltage curve and is not ment to be used to analyze the curves where they bend over due to series resistance. Therefore, the Pt/4H-SiC samples follow theory, even though the ideality factor increases at higher temperatures, because the series resistance effect nullifies the theoretical basis to the ideality factors. In agreement with theory, the ideality factor ranges decreased with higher temperature, as shown in Figures 25 and 26, from n=2.3 to 1.0 for the Ni/6H-SiC samples and from n=3.4 to 1.6 for the Pt/4H-SiC samples. Thus, the 4H-SiC samples had a larger

tunneling component, probably caused by reactions between the metal and the carbon face of the crystal. The ideality factors obtained at 100, 300, and 698 K, respectively, for each sample was 2.97, 1.63, and 3.16 for Pt/4H-SiC Schottky #1, 2.53, 2.07, and 3.13 for Pt/4H-SiC Schottky #2, 2.27, 1.21, and 1.02 for Ni/6H-SiC Schottky #1, 1.40, 1.08, and 1.00 for Ni/6H-SiC Schottky #2, and 1.82,1.08, 1.01 for Ni/6H-SiC Schottky #3. All ideality factors listed have an error of ± 0.05. These values, along with the other current-voltage results, are summarized in Table IV at the end of this section. The series resistance was estimated by fitting a line to a plot of current (non-logarithmic) versus voltage for higher (1.9-2.0 V) voltages. The inverse of the slope yielded the resistance. The 4H-SiC devices had a higher series resistance impact in the current-voltage curves than the 6H-SiC devices, as shown in Figures 20 thru 24, which was suspected to be a result of the diodes being carbon face devices. However, the resistance per area results at room temperature of the 4H-SiC samples were found to be lower than that of the 6H-SiC samples. With measurements yielding: 7.6 and 8.7 x10^4 Ω/cm^2 (± 0.1x10^4 Ω/cm^2) for Pt/4H-SiC Schottky diodes #1 and #2, respectively, and 3.8, 3.3, and 2.8 x10^5 Ω/cm^2 (± 0.1x10^5 Ω/cm^2) for the Ni/6H-SiC Schottky diodes #1, #2, and #3, respectively. Therefore, the higher series resistance values for the 4H-SiC versus 6H-SiC samples come about at higher temperatures, indicating increased chemical activity with the carbon faced contact and a larger bulk resistance with higher temperature These results are summarized in Table IV.
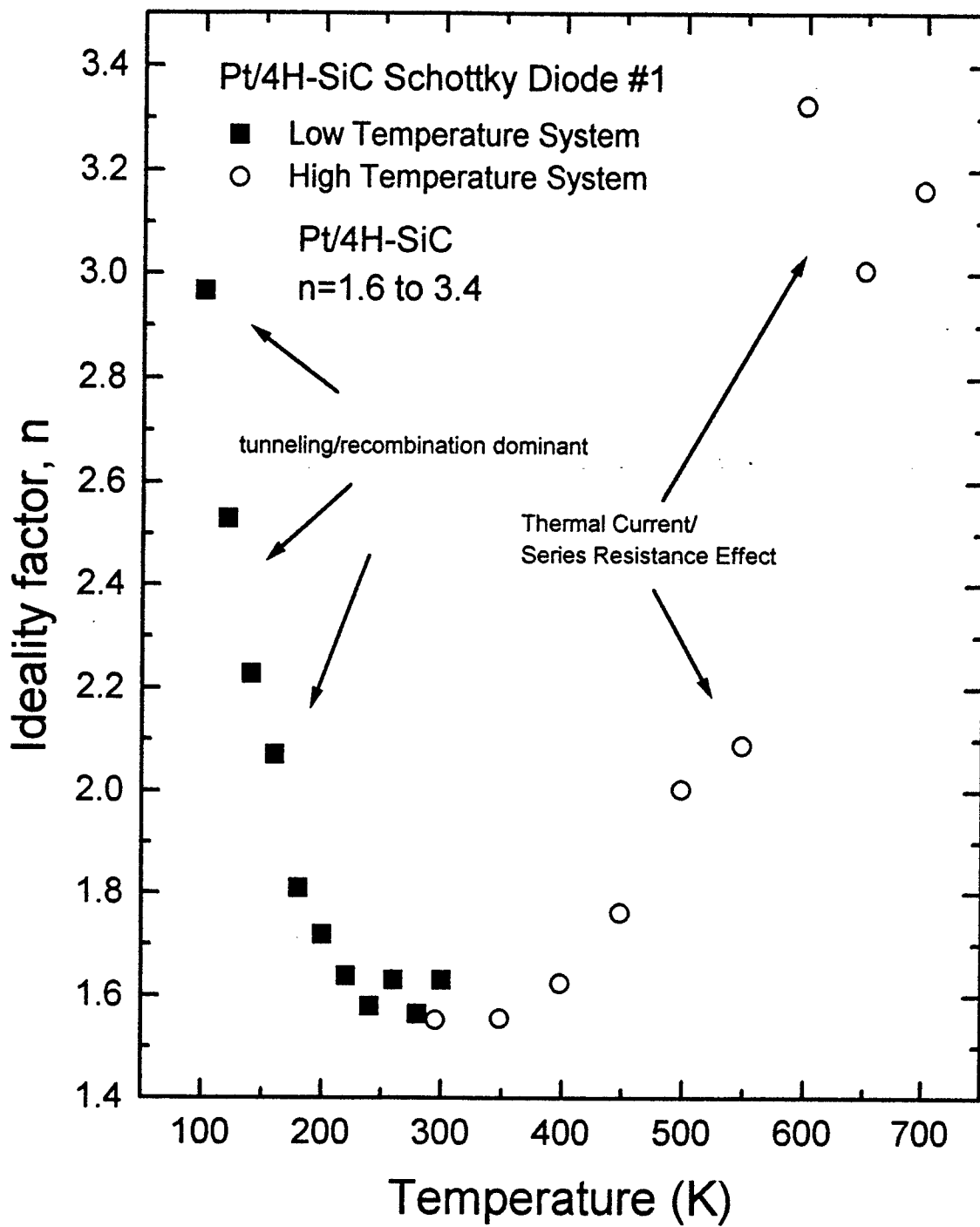
Figure 26. Plot of the ideality factor versus temperature for Pt/4H-SiC Schottky diode #1.

Besides the ideality factors, the linear portion of the natural log of current versus voltage also yielded the saturation currents. The saturation current, I_S, was found from the intercept on the current axis of the current-voltage curves. A plot utilizing equation (4.1) and the calculated saturation currents at different temperatures yielded the barrier height and effective Richardson's constant-active area product. Figures 27 and 28 show the plots of $Ln(I_S/T^2)$ vs $1000/T$ for the devices tested. Although, the values for the Schottky barrier heights and the effective Richardson's constant-active area products were calculated for both the low and high temperature systems, only the values for the high temperature system are reported here. This is because the linear relationship is stronger at higher temperatures, where thermionic emission currents dominate. The Schottky barrier heights determined from these plots, as shown in Figures 27 and 28, are 0.61 and 0.32 eV ($\pm$ 0.05 eV) for 4H/SiC samples #1 and #2, respectively, and 1.10, 1.13, and 1.08 eV ($\pm$ 0.05 eV) for Ni/6H-SiC samples #1, #2, and #3, respectively. The effective Richardson's constant-active area products determined from these plots are 0.094 and 2.8×10^{-4} A/K (amps/Kelvin) for 4H/SiC samples #1 and #2, respectively, and 0.031, 0.167, and 0.0216 A/K for Ni/6H-SiC samples #1, #2, and #3, respectively. These values are summarized in Figures 27 and 28, and in Table IV.

The obtained Schottky barrier heights for the Ni/6H-SiC samples were very close to that shown in Table II. The Ni/6H-SiC Schottky barrier height values ranged from 1.08 eV to 1.13 eV, where a value of about 1.2 eV was expected. An expected Schottky barrier height for the Pt/4H-SiC was obtained by using the workfunction of platinum and the obtained "a" and "b" values from Chapter 3 in equation (3.8). The expected Schottky

barrier height obtained from this calculation was, $\phi_B = 1.9$ eV. Thus, the obtained Schottky barrier heights for the 4H/SiC samples of 0.61 and 0.32 eV were lower than expected. This could be due to surface states causing Fermi level pinning. Each sample has different surface properties because of the different locations on the wafer due to irregularities in growth and metal deposition, and thus the number of surface states will vary. Therefore, the "pinned" barrier heights can occur at different values for the same type of contact. Two possible sources for the surface states are that the samples are carbon faced contacts and platinum silicides may have formed at the interface. Either reason may have caused the density of surface states to become so large that it pinned the barrier height.

Using the values obtained for the Richardson's constant-active area products, an experimentally determined Richardson's constant can be found.. Assuming that the entire physical area of the diodes is active, the effective Richardon's constant-active area values obtained from the $Ln(I_s/T^2)$ plots yielded very much smaller Richardson's constants than the predicted values of 143 and 206 A/cm^2/K for 4H- and 6H-SiC, respectively. These experimentally determined Richardson's constants for 4H-SiC devices #1 and #2 were 1.06×10^{-2} A/cm^2/K and 3.18×10^{-5} A/cm^2/K, respectively. For the 6H-SiC devices they were 2.01×10^{-2} A/cm^2/K, 9.33×10^{-2} A/cm^2/K, and 1.07×10^{-2} A/cm^2/K for devices #1, #2, and #3 respectively. These extremely small values indicate that the active areas of the contacts are much smaller than device areas, that the quantum mechanical effects are affecting the Richardson's constant as shown in equation (3.36), or that there is a combination of the two effects.
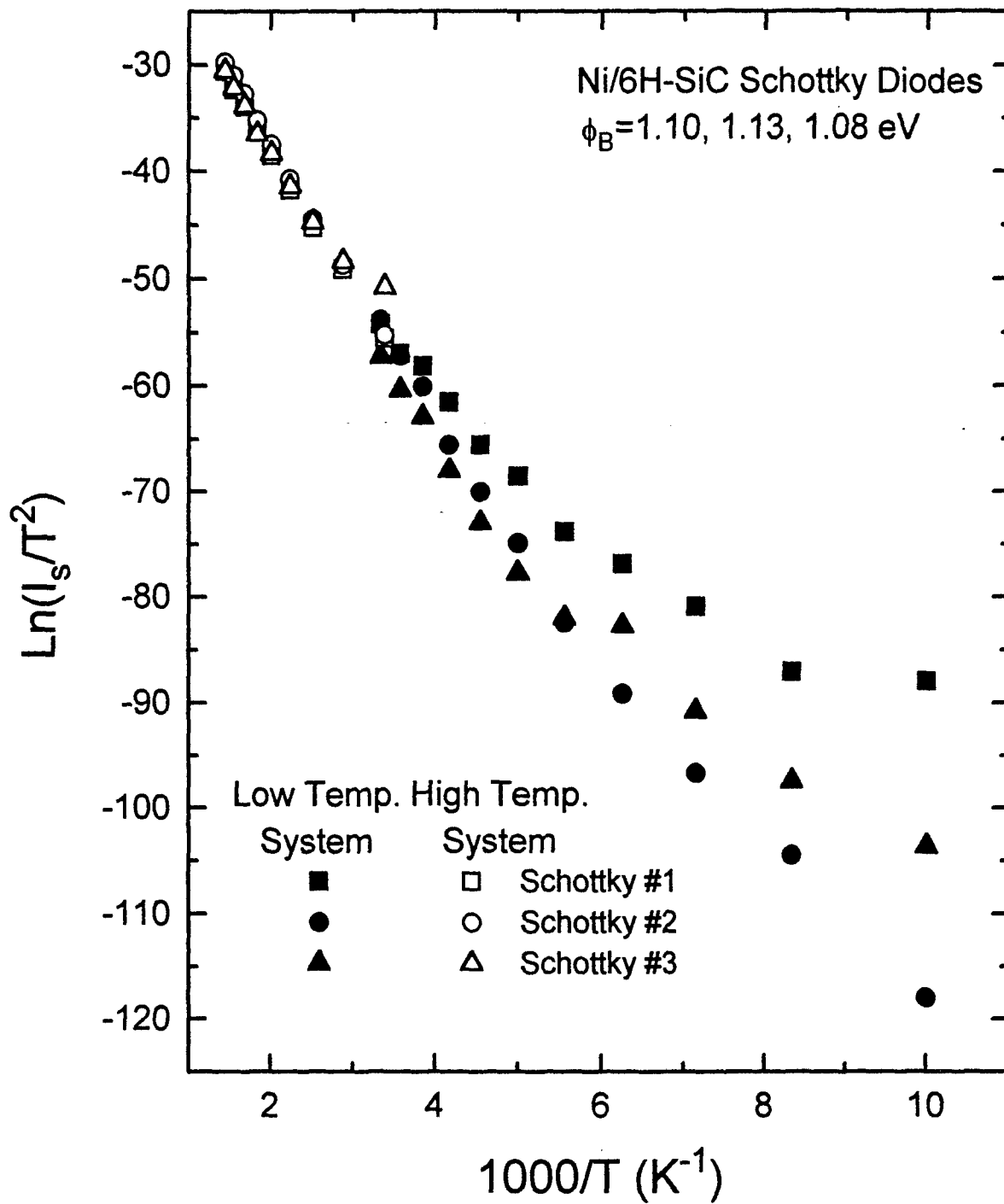
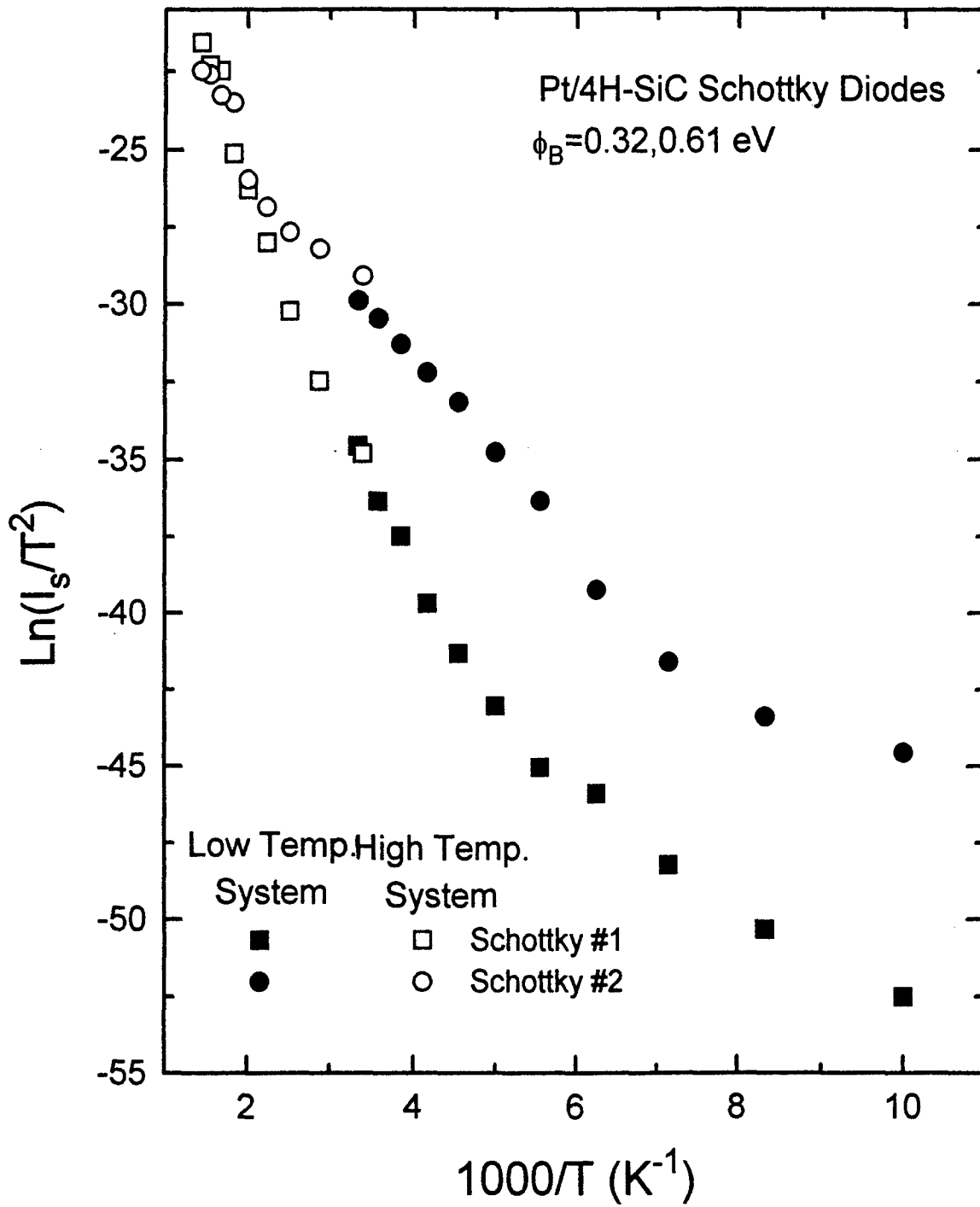Figure 27. Ln(I_S/T^2) vs 1000/T plot for the Ni/6H-SiC Schottky diode samples.

Figure 28. Ln(I_S/T^2) vs 1000/T plot for the Pt/4H-SiC Schottky diode samples.

A typical reverse current-voltage plot is shown in Figure 29. From the reverse current measurements, it was found that the devices were able to operate at -100 V reverse bias at 698 K without breaking down. The reverse current was found to increase for higher temperatures and voltages due to increased recombination currents and Schottky barrier lowering. The Ni\6H-SiC Schottky diode samples performed very well, passing only microamps of current at -100V and 698 K. The 4H-SiC samples however allowed currents in the milliamp range at -100V and 698 K. The reverse current-voltage characteristics also allowed for determination of the activation energies of the traps in the SiC material as given by equation (4.7). However, due to the presence of surface states, edge leakage currents, or multiple deep level traps, activation energies obtained from reverse current, capacitance frequency, or DLTS can be very different from trap activation energies in the bulk material. It is preferable to compare results from all three methods to distinguish actual activation energies from false readings. Therefore the reverse-current, capacitance-frequency, and DLTS results are discussed together at the end of this chapter.
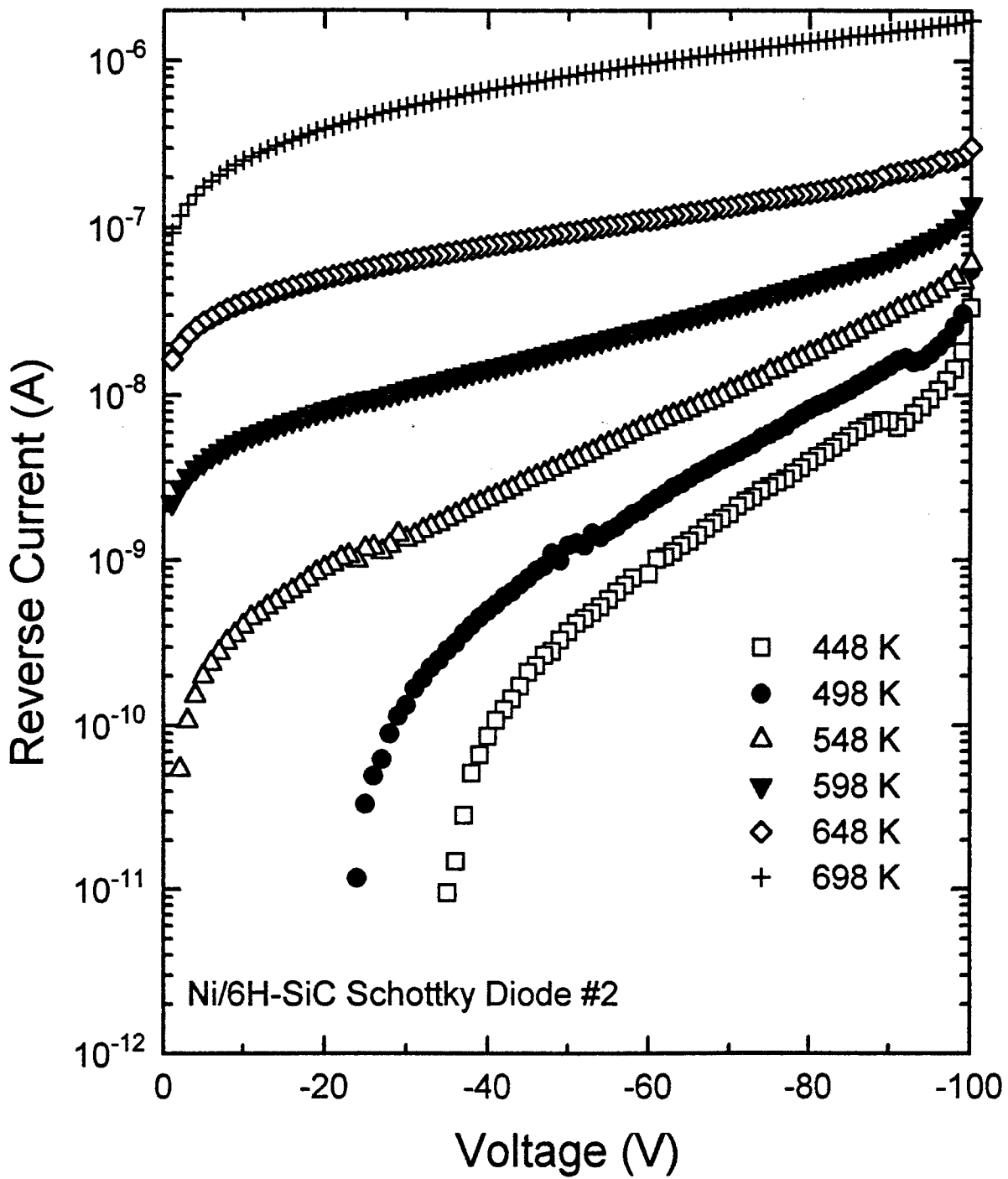
Figure 29. Reverse current-voltage curves at high temperature for Ni/6H-SiC Schottky diode #2.

Table IV. Summary of current-voltage results for both Pt/4H- and Ni/6H-SiC Schottky diodes.

	Pt/4H-SiC Schottky #1	Pt/4H-SiC Schottky #2	Ni/6H-SiC Schottky #1	Ni/6H-SiC Schottky #2	Ni/6H-SiC Schottky #3
ideality factor (n) 100K ($\pm$ 0.05)	2.97	2.53	2.27	1.40	1.82
ideality factor (n) 300K ($\pm$ 0.05))	1.63	2.07	1.21	1.08	1.08
ideality factor (n) 698K ($\pm$ 0.05)	3.16	3.13	1.02	1.00	1.01
series resistance/area at 300K	$7.6 \times 10^4 \pm$ $10^3 \ \Omega/cm^2$	$8.7 \times 10^4 \pm$ $10^3 \ \Omega/cm^2$	$3.8 \times 10^5 \pm$ $10^4 \ \Omega/cm^2$	$3.3 \times 10^5 \pm$ $10^4 \ \Omega/cm^2$	$3.3 \times 10^5 \pm$ $10^4 \ \Omega/cm^2$
Schottky Barrier Height from $Ln(I_s/T^2)$ (in eV) ($\pm$ 0.05 eV)	0.61	0.32	1.10	1.13	1.08
AA** (A/K)	9.4×10^{-2}	2.8×10^{-4}	3.1×10^{-2}	1.67×10^{-1}	2.16×10^{-2}

5.2 Capacitance-Voltage-Temperature (C-V-T)

Capacitance-voltage measurements using equations (4.10) and (4.11) yielded carrier concentrations and barrier heights. Figure 30 shows a typical $1/C^2$ vs. V plot, where C is now the actual capacitance measured, and is not the capacitance per unit area used in equation (4.10). The slopes and voltage intercepts were calculated for three portions of the $1/C^2$ curve for both the 100 KHz and 1 MHz frequencies. The voltage ranges used were 1.95 to 5.85V, 5.85-11.7V, and 13.65-19.5V. The obtained estimates of carrier concentration as a function of temperature for the low voltage range at two

different frequencies are plotted in Figure 31. The obtained estimates of carrier concentration as a function of temperature for the three voltage ranges are plotted in Figure 32. The 1 MHz capacitance and carrier concentration results were found to be slightly smaller than for the 100 KHz bias signal. This was due to the fewer numbers of carriers excited by the 1 MHz signals (see Figure 31). The $1/C^2$ slopes for the higher voltages were found to be flatter, thus carrier concentrations, which are inversely proportional to the slope, were higher. This increase in carrier concentration versus voltage was caused by the widening of the depletion region at the higher voltages. It was also found that the carrier concentrations did stay relatively constant as the temperature varies, as predicted by theory (see Figure 32). The carrier concentrations obtained at the larger voltages were found to be noisier due to the sensitivity of capacitance measurements to carrier concentration. For better comparison with the forward current-voltage results, the lower voltage range was used, as the depletion widths and barrier heights would be similar. The carrier concentration results for the 1.95-5.85V range at 1 MHz are given in Table V. The Ni/6H-SiC samples were found to have carrier concentrations ~5 times as great as the Pt/4H-SiC samples.
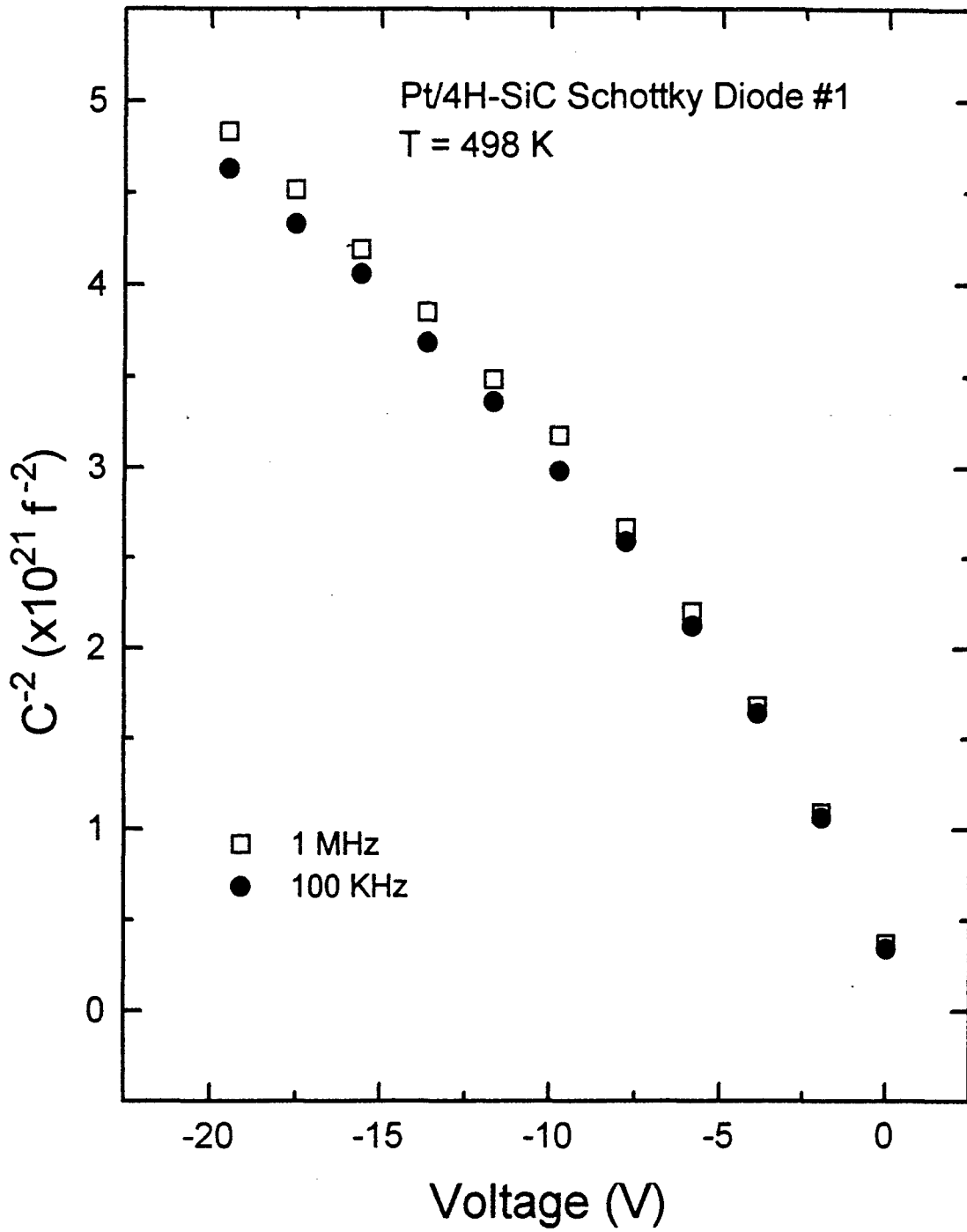
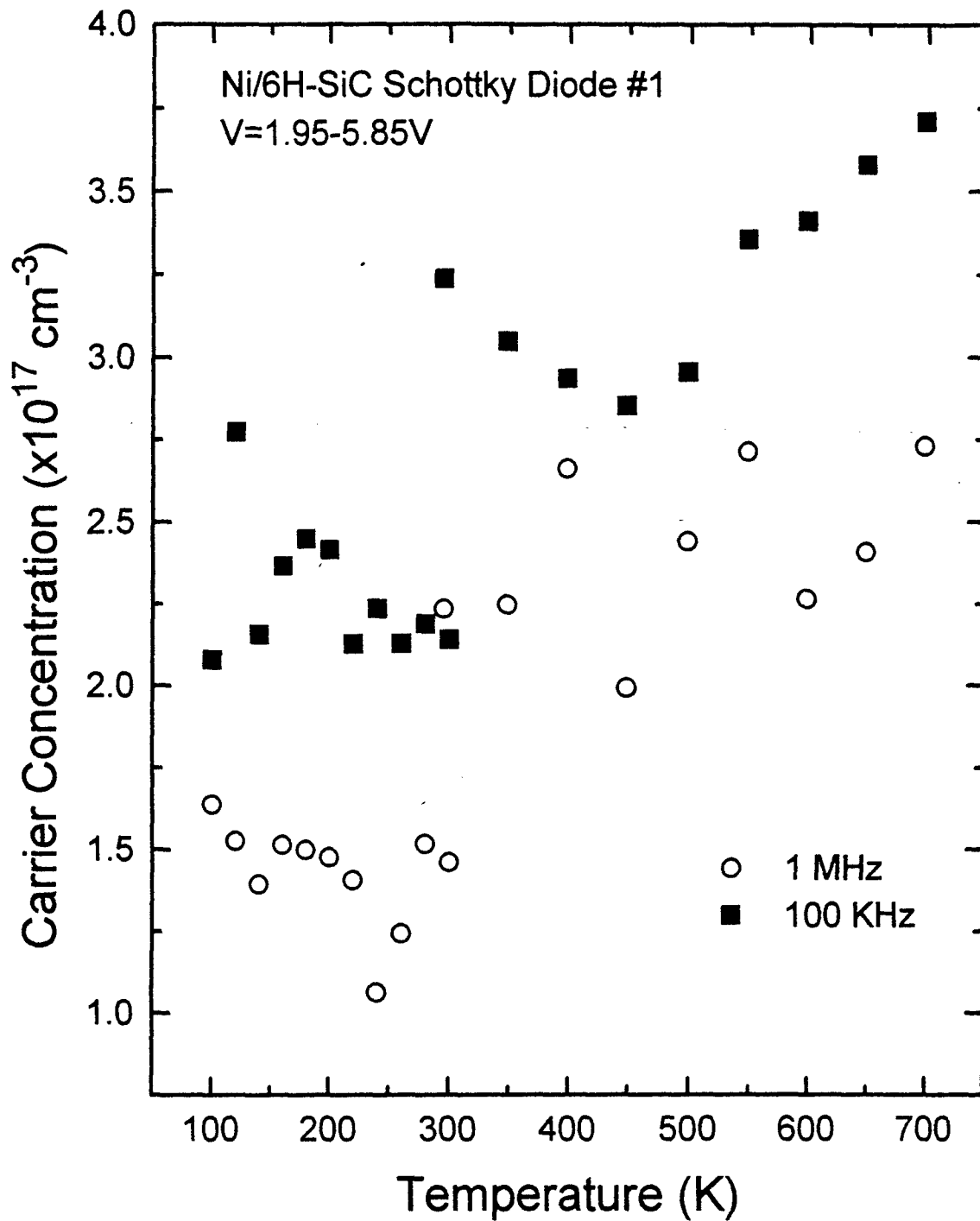Figure 30. Typical $1/C^2$ vs. V plot for Pt/4H-SiC Schottky diode #1.

Figure 31. Plot of carrier concentration vs. temperature at two different frequencies for Ni/6H-SiC Schottky diode #1.
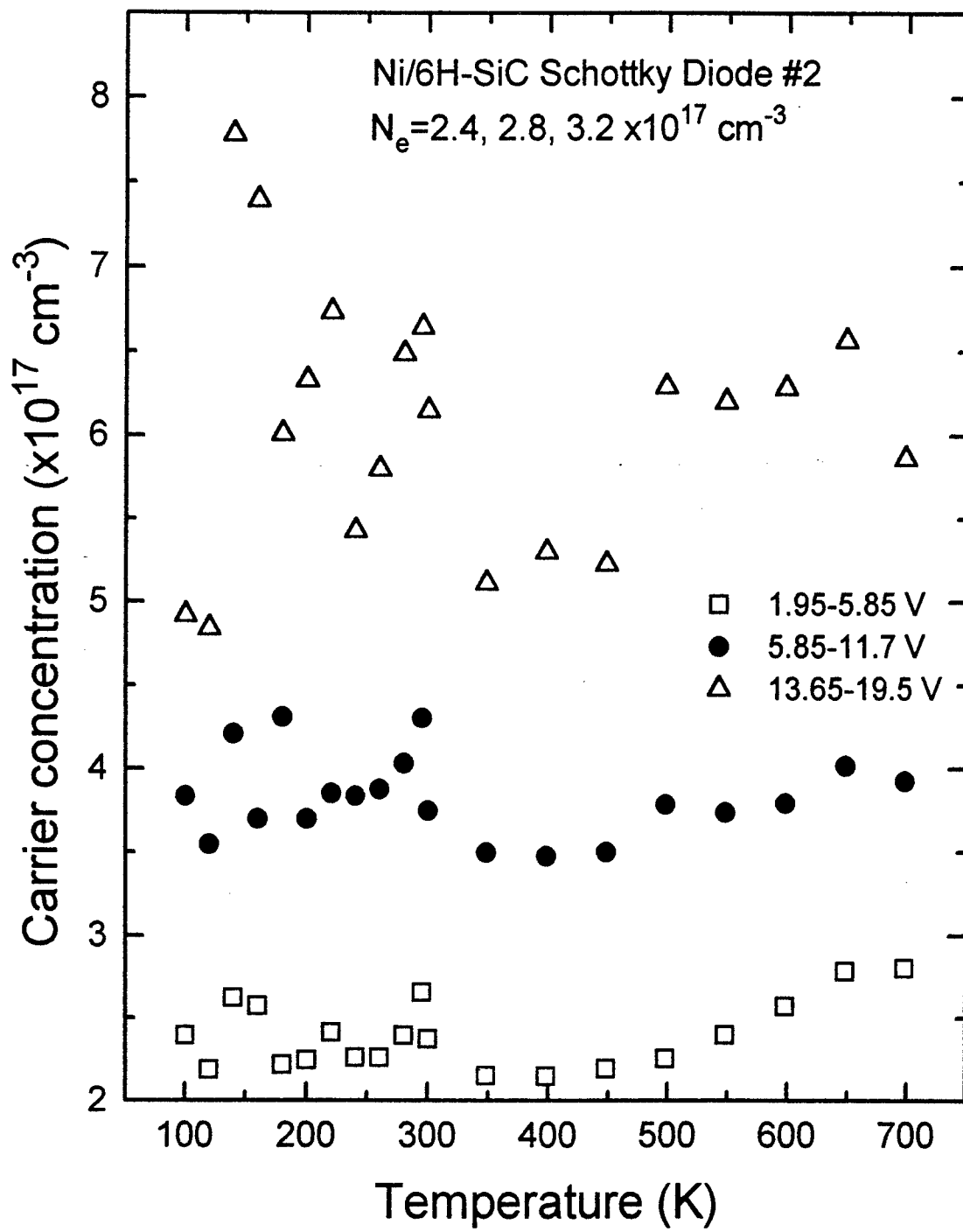
Figure 32. Plot of carrier concentration vs. temperature for three reverse bias voltage ranges for the Ni/6H-SiC Schottky diodes.

The Schottky barrier heights were obtained from the intercept of the $1/C^2$ lines on the voltage axis as shown by equation (4.11). It was found that the barrier heights increased dramatically with the increased voltage due to band bending. It was also found that for the 4H/SiC samples, the barrier height, like the carrier concentration, stayed relatively constant versus temperature, but at high temperatures the heat acted as a forward bias, lowering the barrier height as shown in Figure 33. Due to the higher carrier concentrations, the barrier height results for the 6H/SiC samples were very noisy. The barrier heights determined from the capacitance-voltage measurements are given in Table V. The values are greater than those found from current-voltage tests because of the reverse voltage lowering of the barrier height coupled with the sensitivity of the capacitance measurements to any defects.

Table V. Summary of capacitance-voltage results

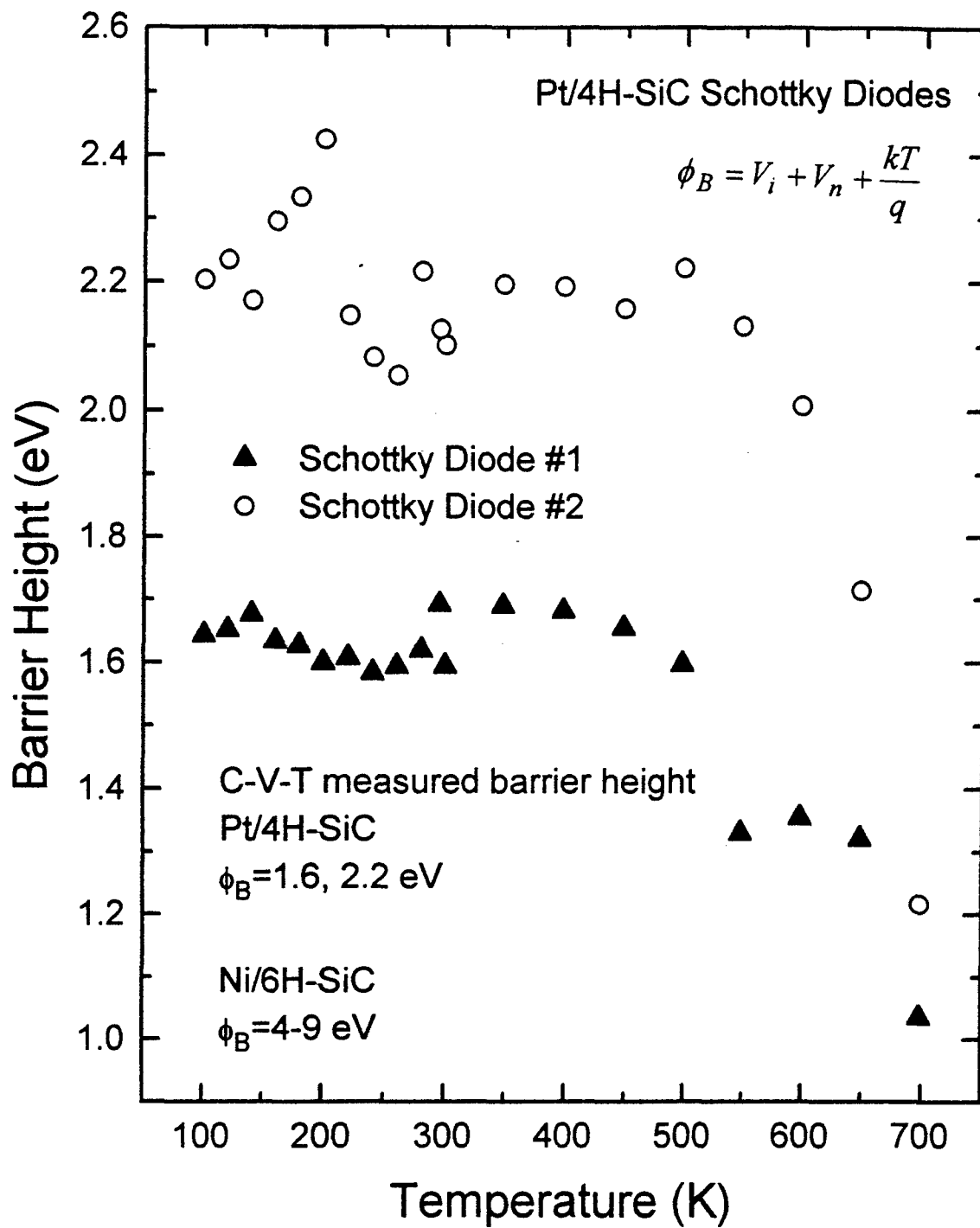|	Pt/4H-SiC Schottky #1	Pt/4H-SiC Schottky #2	Ni/6H-SiC Schottky #1	Ni/6H-SiC Schottky #2	Ni/6H-SiC Schottky #3
Carrier concentration (1.95-5.9V) ($\times 10^{16}$ cm^{-3})	6.0 ± 0.5	4.8 ± 0.1	25 ± 3	28 ± 6	33 ± 3
Schottky Barrier Heights from $1/C^2$ (eV)	1.6 ± 0.2	2.2 ± 0.2	5.5 ± 1.5	5.9 ± 2.1	7.4 ± 1.3

Figure 33. Plot of barrier height vs. temperature for the Pt/4H-SiC Schottky diodes.

5.3 Activation Energy Experiments (reverse current, capacitance-frequency, and DLTS)

Reverse-current, capacitance frequency, and DLTS experiments all yielded activation energies of traps in the semiconductor material. As mentioned, the methods are very sensitive to any defects present, thus to remove false signals, results are compared with each other and matching activation energies are reported.

Figure 34 shows a typical plot of the log of the reverse current versus 1/kT. From the negative of the slopes for the different linear regions, the activation energies at different bias voltages were obtained, as per equation (4.7). It was found that the slopes, thus activation energies, decreased with bias voltage. This is due to the reduction in the barrier height from the Schottky effect and the energy band bending in the semiconductor. As the band is bent, carriers located at trap sites within the semiconductor are able to tunnel or recombine with carriers from the metal through the narrow region (see Figure 17).

Activation energies were obtained from capacitance-frequency measurements at 9.5 V reverse bias at different temperatures. Figure 35 shows one of the resulting dC/dT plots. The peaks in the 1 MHz lines occurred at higher temperatures as predicted by theory. Using equation (4.12) and the values for the two temperatures at which the peaks occur, the activation energies are found. Figure 36 shows a typical Arrenhius analysis of a DLTS signal. Using equation (4.17), linear fitting the lines yielded the activation energies from the slopes.
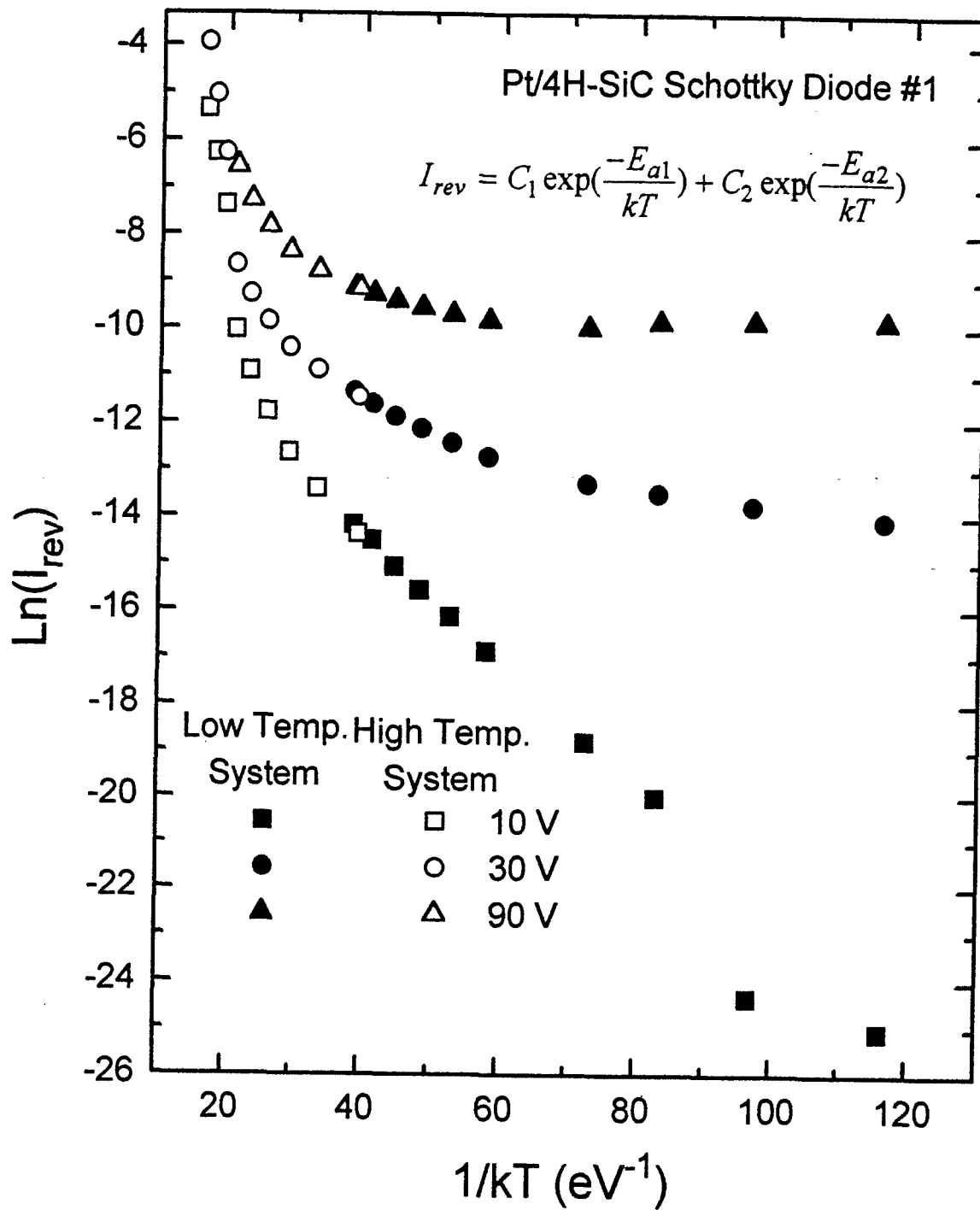
Figure 34. Reverse current activation energy plot for different bias voltages for Pt/4H-SiC Schottky diode #1.
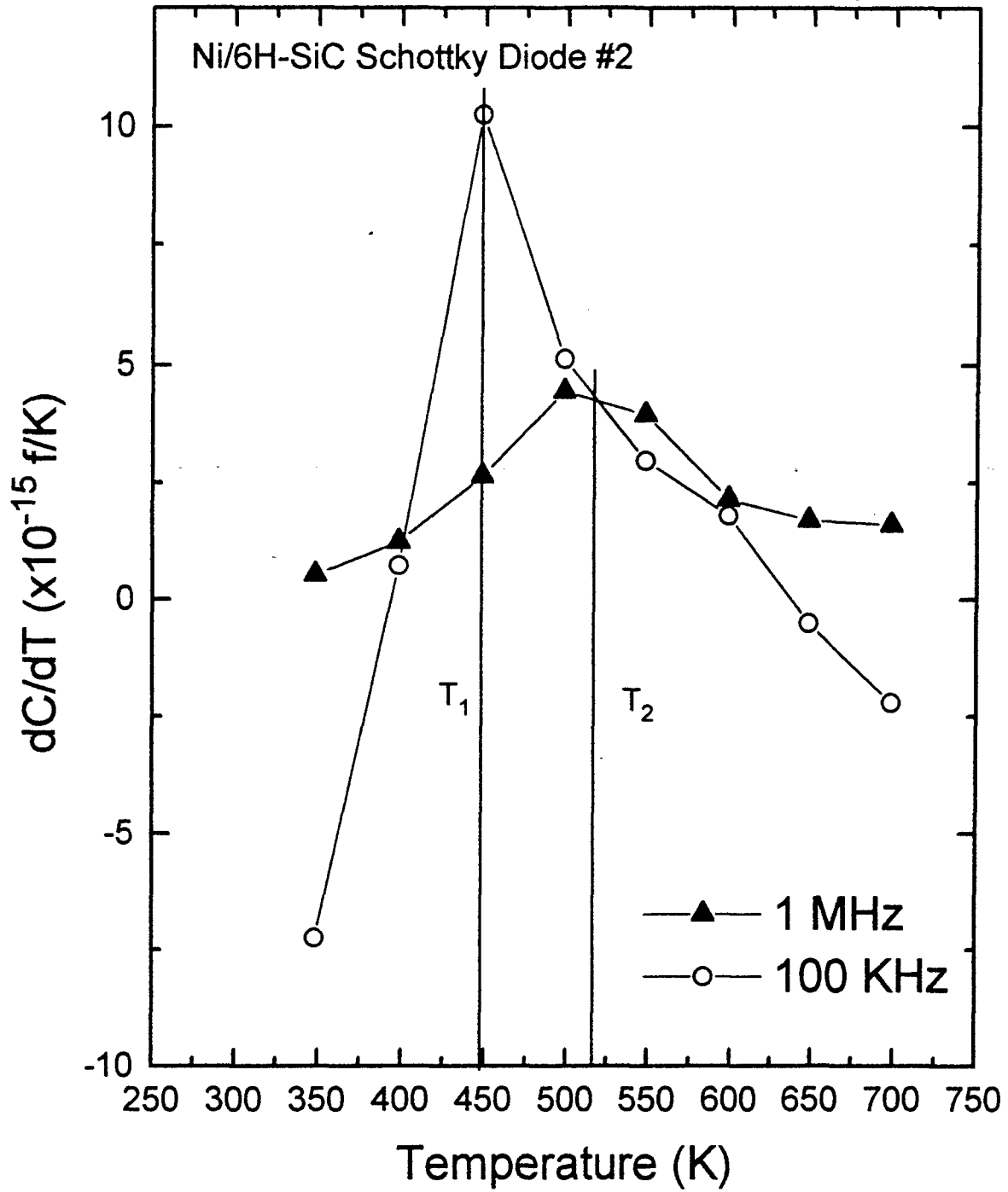
Figure 35. Typical dC/dT plot. Activation energies are obtained from the temperatures at which the peaks occur.

94

Arrhenius Analysis Pt/4H-SiC:Schottky #1

$$\frac{e_p}{T^2} = \sigma(\infty)\exp\left(-\frac{E_a}{kT}\right)$$

Legend:
- ■ 268 meV
- □ 50 meV
- ● 504 meV
- ○ 147 meV
- ▲ 1.4 eV
- × 730 meV

Y-axis: Ln (T^2/e)

X-axis: 1/kT (1/eV)

Figure 36. Arrhenius plot for Pt/4H-SiC Schottky diode #1. Activation energies are obtained from the slopes of the curves.

The activation energies obtained for these three methods were compared and matches were determined. The resulting matched activation energies are approximately 50 and 150 meV and 50, 150, and 450 meV for Pt/4H-SiC samples #1 and #2, respectively, and aprroximately 400, 300, and 300 meV for Ni/6H-SiC samples #1, #2, and #3, respectively. These results are summarized in Table VI along with the activation energy values from each method that indicated these results.
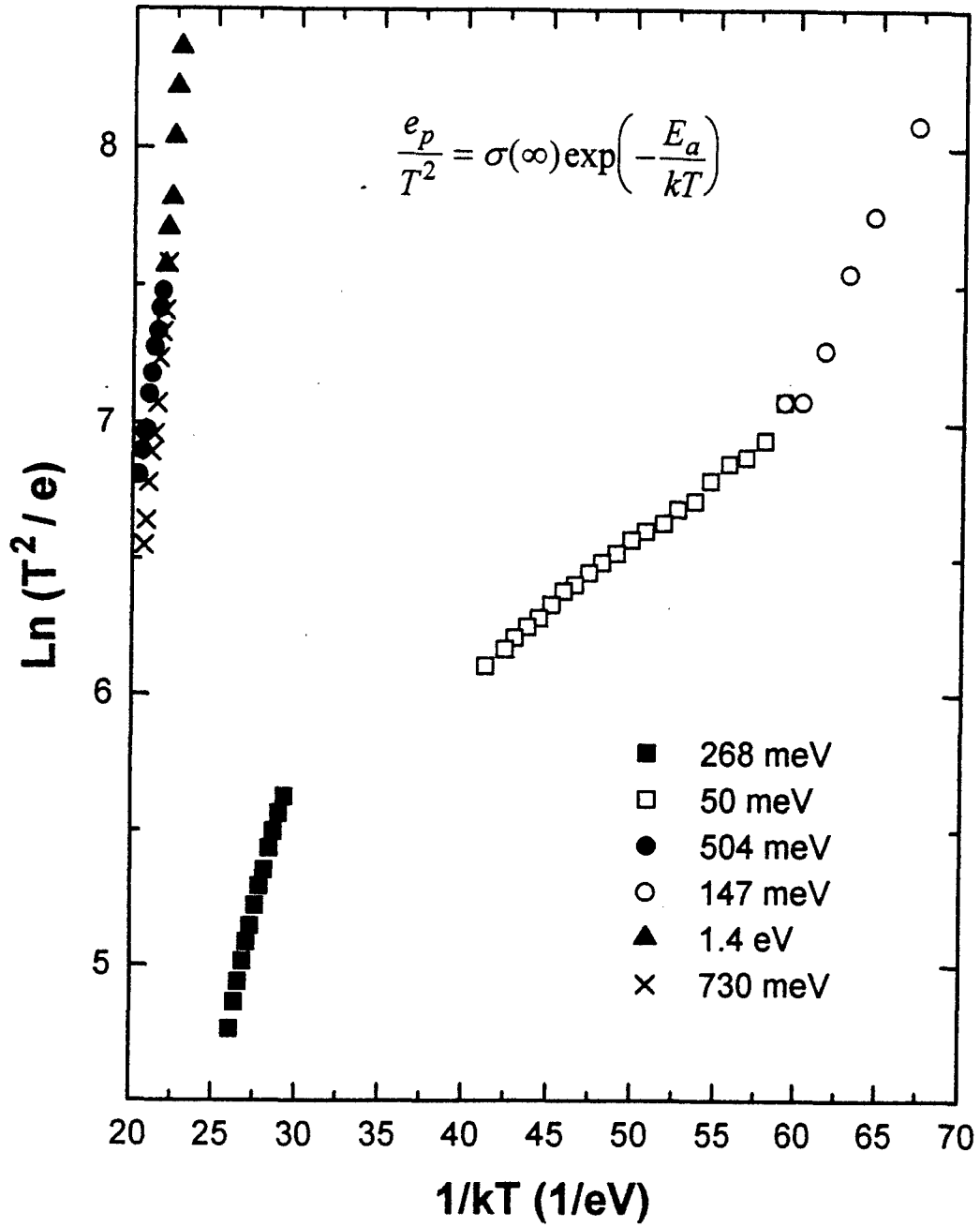
Table VI. Matched activation energies (meV)

	Pt/4H-SiC Schottky #1	Pt/4H-SiC Schottky #2	Ni/6H-SiC Schottky #1	Ni/6H-SiC Schottky #2	Ni/6H-SiC Schottky #3
Reverse current (10V)	38, 133, 169	38, 136, 553	416	287	
C-F-T (9.5V)	173	55		254, 338	330
DLTS	50, 147	66,173, 407	455	317	353
Result	~50, ~150	~50, ~150, ~450	~400	~300	~300

The 50 meV activation energy of the 4H-SiC samples was attributed to the nitrogen donor in the hexagonal (h) site. The other activation energy levels were not identified.

5.4 Breakdown Voltage Tests

Breakdown voltage studies were first performed on the 6H-SiC diodes at room temperature. Breakdown tests before the Fluorinert was applied resulted in a breakdown

voltage of approximately 500 V. After the Fluorinert was applied the breakdown voltage increased to about 800 V. A new batch of Fluorinert was ordered and the tests were performed on the 4H-SiC samples. With these samples the breakdown voltage before Fluorinert was about 140 V. Application of Fluorinert did not increase the breakdown voltage, however reverse currents were increased. Forward and reverse current measurements were taken at room temperature before and after application of the Fluorinert, and definite increase in reverse current while the breakdown point remains the same was seen. This indicated that the Fluorinert had become contaminated, and the diode was more conducting due to increased surface currents.

6. Conclusions and Recommendations

A theoretical and background review of silicon carbide and Schottky contacts was given. The importance of processing techniques in the formation of Schottky contacts was presented. Two Pt/4H-SiC and three Ni/6H-SiC Schottky diodes fabricated by different means were characterized using current-voltage, capacitance-voltage, DLTS, and breakdown voltage experiments. The diodes behaved according to theory, and barrier heights, current conduction mechanisms, carrier densities, activation energies, and breakdown voltages were determined.

For the Pt/4H-SiC Schottky diodes, it was determined from ideality factor and effective Richardson's constant-active area analysis that tunneling and series resistance played a large role in the current processes. These effects are attributed to the fact that the Pt/4H-SiC Schottky contacts are on carbon, rather than silicon faced SiC. Carbon has been shown to be more reactive, and thus barrier heights can become pinned with the presence of many surface states. This led to the measured barrier heights being lower than the expected 1.9 eV. The Pt/4H-SiC devices had barrier heights of 0.61 and 0.32 eV, and 1.6 and 2.2 eV as was determined by current-voltage and capacitance-voltage measurements, respectively. The ideality factors ranged from ~1.6 to 3.2, and the series resistance was found to be approximately 8×10^4 Ω/cm^2. Capacitance measurements yielded a carrier concentration of about 5×10^{16} cm^{-3}, which agrees with the doping density of ~4×10^{16} cm^{-3} specified by the contractor. Reverse current-voltage, capacitance frequency, and DLTS gave trap activation energies of ~50, 150, and 450 meV. The 50

98

meV activation energy is attributed to the nitrogen donor in the hexagonal (h) site. The breakdown voltage was found to be ~140 V.

With the Ni/6H-SiC samples, tunneling effects were not as great as shown by ideality factor analysis, which yielded an ideality factor of 2.3 at low temperature that was lowered from to 1.0 at high temperature, as predicted by theory. The series resistance was about 3.3×10^5 Ω/cm^2 and the Schottky barrier heights of approximately 1.1 eV obtained from current-voltage analysis were in agreement with the value 1.2 eV others had published. C-V-T measurements yielded a carrier concentration of about 2.5-3.0 $\times 10^{17}$ cm^{-3}. This high carrier concentration gave noisy capacitance results, which also gave wide ranging values of barrier heights (4-9 eV). Activation energies were determined to be at about 300 and 400 meV. Breakdown analysis showed an increase in breakdown voltage from ~500 to ~800 V with the application of Fluorinert, indicating the presence of edge and surface leakage currents that could be removed.

Comparing the two types of devices studied was difficult because they were processed differently by separate sources, they were made of different metals, and they were on different substrates. Making devices from carbon faced SiC appeared to have a negative effect in the Pt/4H-SiC samples, as did the high carrier concentration in the Ni/6H-SiC samples. Therefore it is suggested that Schottky contacts made on the silicon face of lesser doped epilayers be studied.

In conclusion, more study of silicon carbide Schottky diodes is recommended to further enhance understanding of the formation mechanisms at work. Results of experiments have only been somewhat consistent as the Schottky contacts have shown a

great sensitivity to the fabrication process. Therefore, different fabrication processes and the contacts they form must be studied. In an aid to this endeavor, electrical characterization of Schottky contacts provides a simple, yet effective means towards completing an overall understanding of the physics of barrier formation. The physics of Schottky contacts must be understood before high temperature/high power devices made of silicon carbide can be made to meet the needs of the U.S. Air Force and the Department of Defense.

References

1. Reinhardt, K.C., et al. "Directions in Air Force High-Temperature Electronics". Internal Paper. Power Semiconductors Division, Wright Laboratory, Wright-Patterson AFB OH.

2. Scofield, J.D. "Electrical Characterization of Acceptor-Impurity Induced Bulk and Interface States in Hexagonal SiC". PhD dissertation prospectus. Department of Engineering Physics, School of Engineering, Air Force Institute of Technology (AU), Wright Patterson AFB OH , December 1993.

3. Morkoç, H. et al. *J. Appl. Phys.* **76**, 1363 (1994).

4. Tairov, Y.M. and Vodakov, Y.A. "Group IV Materials (Mainly SiC*)*", *Topics in Applied Physics: Electroluminescence*, J.I. Pankove ed. Springer-Verlag Berlin Heidelberg, 1977.

5. Reinhardt, K. C. *Study of InP Metal-Semiconductor and Thin Insulator Metal-Insulator-Semiconductor Diodes*. MS thesis. School of Science, State University of New York at Buffalo, Buffalo, NY, June 1988.

6. Steckl, A.J. "Silicon Carbide Schottky Diodes for High Temperature/ High Power Electronics". Proposal to the Ohio Aerospace Institute (May 22, 1995).

7. Liu, S. and Reinhardt, K.C. "Metal Contacts on SiC". Internal Paper. Power Semiconductors Division, Wright Laboratory, Wright-Patterson AFB OH (August 1995).

8. Porter, L. et al. *Mat. Res. Soc. Symp. Proc.* **282**, 471 (1993).

9. Petit, J.B. et al. *Mat. Res. Soc. Symp. Proc.* **242**, 567 (1992).

10. Dmitriev, V.A. et al. in *Amorphous and Crystalline Silicon Carbide IV*. C.Y. Yang, M.M. Rahman, and G.L. Harris eds. Springer-Veralg Berlin Heidelberg , 1992.

11. Spellman, L.M. et al. in *Amorphous and Crystalline Silicon Carbide IV*, Springer Proc. in Phys., Vol. 71. Springer-Veralg Berlin Heidelberg , 1992.

12. Waldrop, J.R. and Grant, R.W. *J. Appl. Phys.* **72**, 4757 (1992).

13. McMullin, P.G. et al. in *Amorphous and Crystalline Silicon Carbide III*, Springer Proc. in Phys., Vol. 56. Springer-Veralg Berlin Heidelberg, 1992.

14. Waldrop, J.R. and Grant, R.W. *Appl. Phys. Lett.* **62**, 2685 (1993).

15. Itoh, A. et al. *IEEE Electron. Dev. Lett.* **16**, 280 (1995).

16. Raghunathan, R. et al. *IEEE Electron Dev. Lett.* **16**, 226 (1995).

17. Taylor, A. and Jones, R.M. "The Crystal Structure and Thermal Expansion of Cubic and Hexagonal Silicon Carbide", *Silicon Carbide, A High Temperature Semiconductor*. J.R. O'Connor and J. Smiltens, eds. Pergamon, 1960.

18. Jepps, N.W. and Page, T.F. "Polytypic transformations in Silicon Carbide", *Progress in Crystal Growth and Characterization, Vol. 7-- Crystal Growth and Characterization of Polytype Structures*, P. Krishna, ed. NY: Pergamon, 1983. pp. 259-307.

19. *Semiconductors: Group IV Elements and III-V Compounds*. O. Madelung, ed. Springer-Verlag Berlin Heidelberg, 1991.

20. Junginger, H.G. and van Haeringen, W. *Phys. Stat. Sol.* **37**, 709 (1970).

21. Gavrilenko, V.I. et al. *Phys. Stat. Sol.(b)* **162**, 477 (1990).

22. Götz, W. et al. *J. Appl. Phys.* **73**, 3332 (1993).

23. Pensl, G. and Choyke, W.J. *Physica B* **185**, 264 (1993).

24. Lely, J.A. *Ber. Deut. Keram. Ges.* **32**, 229 (1955).

25. Davis, R.F. et al. *Proc. of the IEEE* **79**, 677 (1991).

26. Westinghouse STC. *Technology for High Temperature Electronics: SiC for X-Band.* Annual Report. Pittsburg: Westinghouse STC, April 1994.

27. Tairov, Y.M. and Tsverkov, R. *J. Cryst. Growth* **52**, 146 (1981).

28. Palmour, J.W. et al. "Silicon Carbide Substrates and Power Devices", *Proc. 21st Int. Symp. Compound Semiconductors*. Bristol, UK: IOP. (1994).

29. Davis, W. *Photoluminescence Spectroscopy of 4H- and 6H-SiC.* MS Thesis, AFIT/GAP/ENP/94D-2. School of Engineering, Air Force Institute of Technology (AU), Wright-Patterson AFB OH, December 1994.

30. Neudeck, P.G. and Powell, J.A. *IEEE Electron Dev. Lett.* **15**, 63 (1994).

31. Neudeck, P.G. "Progress in Silicon Carbide Semiconductor Electronics Technology", submitted October 1994 to *Journal of Electronic Materials.*

32. Rideout, V.L. *Thin Solid Films* **48**, 261 (1978).

33. Sze, S.M. *Physics of Semiconductor Devices, 2nd. ed.* John Wiley and Sons, 1981.

34. Michaelson, H.B. *J. Appl. Phys.* **48**, 4729 (1977).

35. Bethe, H.A. *M.I.T. Radiat. Lab. Rep. 43-12* (1942).

36. Crowell, C.R. *Solid St. Electron.* **8**, 395 (1965).

37. Schottky, W. *Naturwissenschaften*, **26**, 843 (1938).

38. Crowell, C.R. and Sze, S.M. *Solid St. Electron.* **9**, 1035 (1966).

39. Crowell, C.R. and Sze, S.M. *J. Appl. Phys.* **37**, 2683 (1966).

40. Sze, S.M. et al. *J. Appl. Phys.* **35**, 2534 (1964).

41. Scharfetter, D.L. *Solid St. Electron.* **8**, 299 (1965).

42. Chang, C.Y. et al. *Solid St. Electron.* **14**, 541 (1971).

43. Evwaraye, A. et al. *J. Appl. Phys.* **74**, 5269 (1994).

44. Chaudhry, M.I. et al. *Int. J. Electron.* **71**, 439 (1991).

45. Waldrop, J.R. and Grant, R.W. *Appl. Phys. Lett.* **56**, 557 (1990).

46. Yoshida, S. et al. *Appl. Phys. Lett.* **46**, 766 (1985).

47. Daimon, H. et al. *Jap. J. Appl. Phys.* **25**, L592 (1986).

48. Steckl, A.J. and Su, J.N. *IEDM*, 695 (1993).

49. Steckl, A.J. et al. in *Silicon Carbide and Related Materials*, Proc. 5th Conf. Institute of Physics Publishing, 1994.

50. Su, J.N. and Steckl, A.J. "300°C Operation of High Voltage SiC Schottky Rectifier", *High Temp. Elec. Workshop.* Ft. Monmouth, NJ, April 1995.

51. Reinhardt, K.C. *The Junction Characteristics and Currrent Conduction Mechanisms of GaInP$_2$ n$^+$p Diodes and Solar Cells.* PhD dissertation. School of Engineering, Air Force Institute of Technology (AU), Wright-Patterson AFB OH, December 1994.

52. Lang, D.V. *J. Appl. Phys.* **45**, 3023 (1974).

53. Tan, C. and Xu, M. *Solid St. Electron.* **32**, 25 (1989).

54. Elsaesser, D. "Deep Levels in Semiconductors with applications to III-V:RE" Special Studies Paper, Phys 899, School of Engineering, Air Force Institute of Technology (AU), Wright-Patterson AFB OH, September 1990.

Vita

2nd Lieutenant Jeffrey C. Wiemeri ▓▓▓▓▓▓▓▓▓▓▓▓▓▓▓▓▓▓. He graduated from Clay High School in South Bend, Indiana in 1990. Receiving a three and one-half year AFROTC scholarship, he attended the University of Notre Dame du Lac, graduating with a Bachelor of Science in Physics in May 1994. While attending the University of Notre Dame, he was a member of the University of Notre Dame Band and was enrolled with AFROTC Detachment 225. He received a reserve commission upon graduation and was assigned directly to the Air Force Institute of Technology to pursue a Master of Science degree in Engineering Physics. He was married ▓▓▓▓ 1995 to Kiley Elizabeth Coble. He is due to graduate in December 1995 and his tentative follow-on assignment is with Solid State Electronics Lab, Wright Laboratories, Wright-Patterson AFB, OH.

REPORT DOCUMENTATION PAGE

1. AGENCY USE ONLY (Leave blank)	2. REPORT DATE	3. REPORT TYPE AND DATES COVERED
	December 1995	Master's Thesis

4. TITLE AND SUBTITLE

Electrical Characterization of 4H- and 6H-Silicon Carbide Schottky Diodes

5. FUNDING NUMBERS

6. AUTHOR(S)

Jeffrey C. Wiemeri
2nd Lt, USAF

7. PERFORMING ORGANIZATION NAME(S) AND ADDRESS(ES)

Air Force Institute of Technology, WPAFB OH 45433-6568

8. PERFORMING ORGANIZATION REPORT NUMBER

AFIT/GAP/ENP/95D-16

9. SPONSORING/MONITORING AGENCY NAME(S) AND ADDRESS(ES)

Dr. Kitt C. Reinhardt
WL/POOC
Wright Laboratories
Wright-Patterson AFB, OH 45433-6543

10. SPONSORING/MONITORING AGENCY REPORT NUMBER

11. SUPPLEMENTARY NOTES

12a. DISTRIBUTION/AVAILABILITY STATEMENT

Approved for public release; Distribution Unlimited

12b. DISTRIBUTION CODE

A

13. ABSTRACT (Maximum 200 words)

The current conduction mechanisms of n-type 4H- and 6H-SiC with Pt- and Ni-Schottky contacts, respectively, were studied using current-voltage-temperature (I-V-T), capacitance-voltage-temperature (C-V-T), deep level transient spectroscopy (DLTS), and reverse breakdown measurements. The Schottky barrier heights measured from I-V-T are shown to be about 0.3-0.6 and 1.1 eV for the 4H- and 6H-SiC samples, respectively. Current and voltage dependencies of thermionic and field emission current processes are compared to theory. The currents are shown to have a large on-resistance and tunneling component, with ideality factors of n=1.0-3.2, which correlates to the low barrier heights. Capacitance-frequency, current-frequency, and the DLTS data show the presence impurity centers at about 50 and 150 meV in the 4H-SiC samples and about 300 and 400 meV in the 6H-SiC samples. The breakdown voltages of the diodes were found to increase from ~100 V to several hundred volts with the application of Fluorinert, indicating the presence of edge leakage currents.

14. SUBJECT TERMS

Silicon Carbide, Schottky Diodes, Electrical Properties of Semiconductors

15. NUMBER OF PAGES

105

16. PRICE CODE

17. SECURITY CLASSIFICATION OF REPORT	18. SECURITY CLASSIFICATION OF THIS PAGE	19. SECURITY CLASSIFICATION OF ABSTRACT	20. LIMITATION OF ABSTRACT
UNCLASSIFIED	UNCLASSIFIED	UNCLASSIFIED	UL